Tribology International 202 (2025) 110339

Contents lists available at ScienceDirect

Tribology International

journal homepage: www.elsevier.com/locate/triboint

Erosion behavior of Ti-hBN multifunctional coatings in a custom-made planetary test rig at extreme lunar temperatures

Abhijith Kunneparambil Sukumaran [a], Sara Rengifo [b], Brandon Aguiar [a], Sohail M.A.K. Mohammed [a], William Scott [b], Michael Renfro [c], Sang-Hyon Chu [d], Cheol Park [d], Arvind Agarwal [a,*]

[a] Plasma Forming Laboratory, Florida International University, Miami, FL, United States
[b] National Aeronautics and Space Administration, Marshall Space Flight Center, Huntsville, AL, United States
[c] Plasma Processes, Huntsville, AL, United States
[d] Advanced Materials and Processing Branch, NASA Langley Research Center, Hampton, VA, United States

ARTICLE INFO

Keywords:
Lunar dust erosion
Plasma spray coating
Boron nitride
Impact-deformation

ABSTRACT

Spacecraft landings and takeoffs on the lunar surface, along with extreme temperature variations between day and night (−196 to 150º C), cause high-velocity dust impacts and erosion, resulting in the premature failure of structures. Ti/2 vol% hBN coatings were deposited using atmospheric (APS) and vacuum plasma spray (VPS) using cryo-milled powder feedstock to protect the structural components. The erosion performance of coatings at extreme lunar temperature regimes (−150 to 150 °C) was evaluated in a custom-made planetary erosion test rig (PETR) at low (50 mph) and high impact velocities (250 mph). The mass loss of VPS coatings was reduced by 50 % compared to the APS coatings and 40 % compared to the Ti6Al4V substrate. The cryogenic temperature induces brittleness in the material, rendering it susceptible to extreme conditions of material loss. The particle impact-deformation behavior was captured using a high-speed camera to study the erosion mechanism. This analysis revealed chipping in substrates and brittle APS coatings, while particles rebounding and embedding were observed in VPS coatings. Energy calculations, aided by particle trajectory tracking from the high-speed camera, have conclusively shown that VPS coatings absorb 5–10 % more energy than APS coatings during erosion tests. A modified erosion index was developed incorporating the fracture toughness and temperatures. New erosion models for brittle and ductile target materials are proposed for developing erosion-resistant material systems.

1. Introduction

Planetary erosion is a major concern in Lunar and Martian exploration, causing irreparable damage to structural components and rovers [1–4]. The high-velocity regolith impacts generated from exhaust plume impingement and dust storms cause severe material degradation and erosive wear to these lightweight alloys, usually made of Al6061 and Ti6Al4V[5,6]. Severe erosion in the lunar environment is caused by extreme temperatures, vacuum, and solar/cosmic radiation coupled with hard abrasive regolith particles with bi-modal particle size distribution and sharp irregular morphologies[7–9]. Past lunar explorations have caused significant structural damage and health risks to astronauts due to the electrostatic nature of the erosive lunar dust[3,10–12]. Solutions to this glaring problem of dust erosion are inevitable for mission success in the upcoming manned-moon operations such as Artemis and Luna planned over the next few decades to establish the long-term presence and colonization on the moon[13,14].

Previous literature has evaluated the erosion performance of metals such as Al6061 and 1045 steel, polymers such as polycarbonate and polymethyl methacrylate (PMMA), and optical components such as silica glass mostly against JSC-1A lunar simulant at velocities ranging from 50–360 m/s[1,6,15–19]. A detailed review of the lunar erosion studies on different material systems, rigs, and their limitations is discussed in our recent article[3]. Erosive wear on Al6061 alloy by an aerosol generator at 105 m/s impact velocity and 90º impact angle had a profound effect of an 18-fold increase in surface roughness of Al alloy[15]. Erosive wear modeling on Al, steel, and PMMA by the same authors validated their experimental results and found that optical properties

* Correspondence to: 10555 West Flagler Street, EC 3474, Miami, FL 33174, United States.
E-mail address: agarwala@fiu.edu (A. Agarwal).

https://doi.org/10.1016/j.triboint.2024.110339
Received 16 September 2024; Received in revised form 8 October 2024; Accepted 20 October 2024
Available online 24 October 2024
0301-679X/

Table 1
Plasma spray process parameters.

Process Type	Spray distance (mm)	Feeding Type	Primary gas pressure (MPa)	Secondary gas pressure (MPa)	Carrier gas pressure (MPa)	Plasma power (kW)	Deposition time (s)	Vacuum level (MPa)
APS	140	External	0.28 (Ar)	0.55 (He)	0.21 (Ar)	22	90	NA
VPS	100	External	0.69(Ar)	0.34 (He)	0.24 (N_2)	24	90	0.07

such as reflectivity reduced the output current by 40 % in the eroded specimens[17]. The high velocity impacts at 360 m/s from an eddy current accelerator using buckshot quantities of lunar simulants at varying impact angles on Al alloys and silica glass specimens showed a 10-fold increase in roughness where chipping and particle adhesion were identified as the main erosion mechanisms[6]. While most of these studies try to evaluate the effect of optical properties such as reflectivity and transmissivity, none of them have tried to quantify the erosive wear of these specimens or introduced surface protection methods to minimize the erosive wear. Most test setups resort to room temperature testing, while lunar performance assessments require variable temperature regimes.

Hence, this study evaluates the erosive wear behavior of plasma-sprayed novel multifunctional Ti-hBN composite coatings and their efficacy in protecting the lunar structural components in a custom-made planetary erosion test rig. Our recent study has shown that Ti-hBN coatings improve abrasive wear behavior by 90 % against lunar regolith JSC-1A and neutron radiation shielding ability by 27 % [20,21]. The use of hBN due to its inherent properties as a solid lubricant and the formation of hard phases during spraying is shown to improve the hardness thrice compared to conventional Ti6Al4V substrate and enhance wear reduction [20,22]. The ^{10}B isotope with a high neutron absorption cross-section of ~ 3580 barns) enhanced the radiation shielding properties of this coating. In this study, we assess the erosion resistance of coatings using a customized rig to explore their potential as a multifunctional protective solution for both lunar and aerospace applications. In the present study, the erosive wear of Ti-hBN coatings, applied to a Ti6Al4V substrate using atmospheric and vacuum plasma spray methods, are evaluated using a custom-made planetary erosion test rig. This rig simulates extreme lunar thermal fluctuations ranging from −196 to 150 °C and tests the coatings against the JSC-1A lunar simulant. The limitations of previous erosion test rigs were eliminated by introducing a high-speed camera to image the in-situ impact mechanism between the lunar regolith and tested coatings and substrates. The feasibility of using Ti-hBN composite coatings as multifunctional protection for lunar structures was critically evaluated, highlighting them as potential candidates for future dust-mitigating materials.

2. Experimental details

2.1. Materials and coating preparation

Our previous study investigated hBN concentrations of 2 and 10 vol % to evaluate their impact on coating properties. The 2 vol% concentration was optimized based on its superior enhancement of wear resistance and neutron shielding. 10 vol% hBN resulted in BN particle agglomeration and poor powder flowability during plasma spraying, which compromised the structural integrity of the coatings [20]. For the current study, Ti/2 vol% hBN composite powder was prepared from initial powders (hBN: average size = 5 μm, surface area = 7.5 m^2/g, density = 2.1 g/cm^3, sourced from Graphene Supermarket; Ti6Al4V: average size < 30 μm, density = 4.5 g/cm^3, Tekna TEKMAT™ Ti64–45/16-G5; see Fig.S1), through cryomilling. Detailed cryo-milling parameters and coating synthesis procedures can be found in

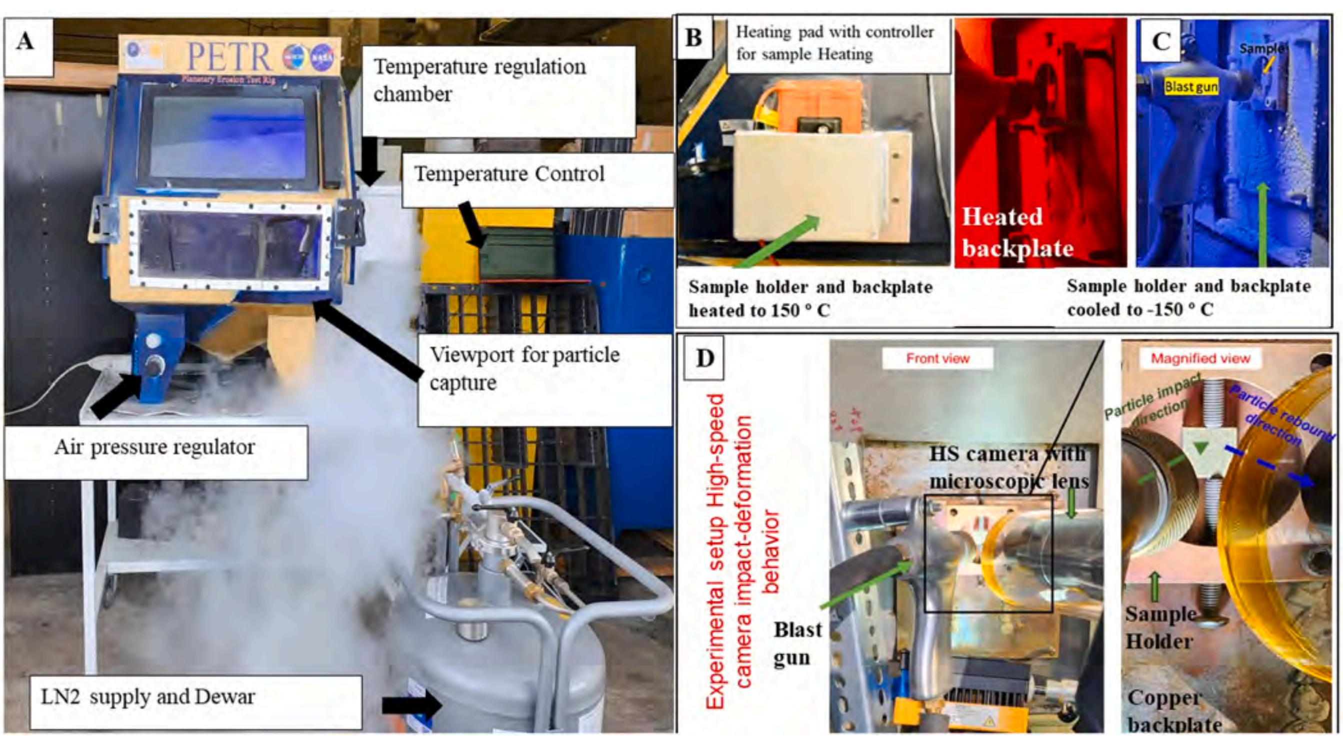

Fig. 1. (A) Planetary Erosion Test Rig (PETR) in low-temperature test condition with cryogenic attachment and temperature control (B) High-temperature test condition with heating pad attached to the back plate (C) Low-temperature test condition with backplate cooled down to –150 °C (D) In-situ impact and deformation behavior capture using high-speed camera and microscopic lens.

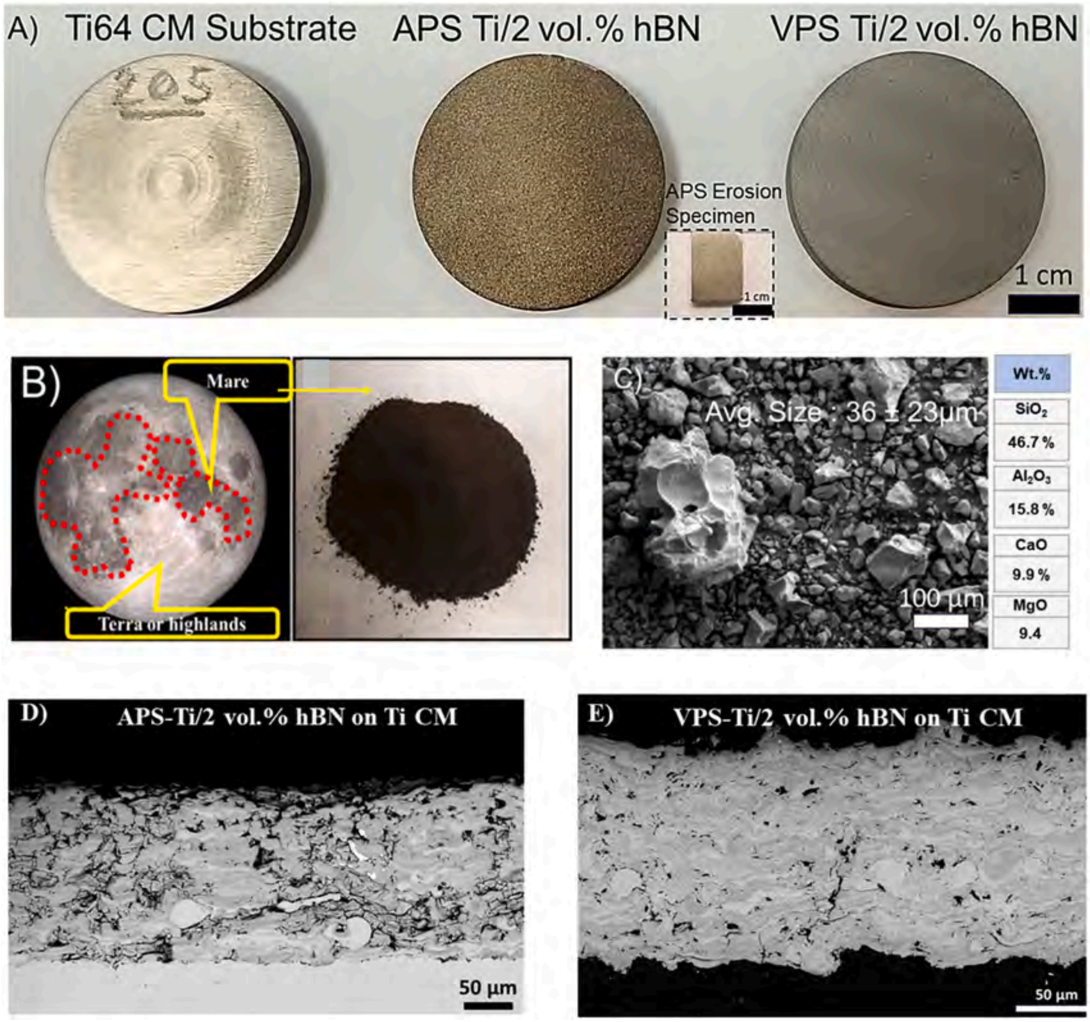

Fig. 2. (A) Uncoated Ti6Al4V substrate, APS Ti/2vol% hBN coating on Ti64 substrate (inset: prepared erosion specimen), and VPS Ti/2vol% hBN coating on Ti64 substrate, (B) JSC-1A lunar simulant represents the lunar mare (ocean), a targeted landing site of Artemis missions, (C) SEM image of microstructure of JSC-1A with sharp edges and bi-modal particle size distribution, (D) SEM image of cross-section of APS Ti/2vol% hBN coating, and (E) SEM image of VPS cross-section of Ti/2vol % hBN coating.

supplementary information and 1.1 of our previous publication[20]. Conventionally manufactured (CM) Al6061 and Ti6Al4V were machined into Φ 3.81 cm × (t) 0.64 cm circular pucks, serving as substrates for APS and VPS coating deposition. The APS coating was deposited at the Plasma Forming Laboratory of Florida International University, while VPS coatings were deposited at Plasma Processes, LLC in Huntsville, Alabama. An SG-100 plasma gun (Praxair Surface Technologies, Indianapolis, Indiana) was used for coating deposition to attain a minimum thickness of 150 μm. Detailed process parameters for coating deposition are provided in Table 1.

2.2. Erosion test setup: planetary erosion test rig (PETR)

The Planetary Erosion Test Rig (PETR) was developed to test the high-velocity impact resistance of metals and composite coatings developed in the Plasma forming laboratory. The erosion rig consists of a sandblast chamber with doors accessible on either side, as seen in Fig. 1 A. The chamber has a compressed air supply, regulator, and a foot pedal system for air input. The chamber also has two rectangular viewports on the side and the top for high-speed camera positioning and impact visualization. The back side of the chamber is attached to the vacuum system to eliminate any residual dust buildup in the system during and after erosion. The right-hand side door of the chamber is made to a sample holder temperature unit assembly out of a 0.25" (6.35 mm) -thick copper slab. One side of the slab has a series of threaded holes to attach to the sample holder. The sample holder is a square-shaped copper slab with two bolts, top and bottom, to ensure the press fits the samples against the copper slab backplate. For low-temperature testing, a specially made aluminum liquid nitrogen container has been provided with a press fit outside the door of the copper backplate. An LN_2 dewar pumps the necessary liquid nitrogen to control the sample temperature at low temperature (LT: −150 °C) through a control valve to the LN_2 container. The temperature of the sample is controlled and regulated using a K-type thermocouple and data logger assembly attached to the back side of the chamber (Fig. 1 A, 1 C). The thermocouple input (K-type, Omega Engineering USA) is connected to the sample holder to monitor the sample temperature with Omega Instruments data logger software. A 120-V, 720-Watt silicone heating pad with a controller.

is used for sample heating (Fig. 1B). The heating pad is attached to the sample-mount-copper back plate assembly with a thermal adhesive. The regulator with the heating pad controls temperature, and a K-type thermocouple and data logger assembly monitor the sample temperature.

Table 2
Erosive wear parameters.

Impact velocity (mph)	Impact Angle	Duration (s)	Temperatures (°C)	Simulant	Standoff (mm)
1. Max:250 ± 20 (112 ± 9 m/s) 2. Min: 50 ± 9 (23 ± 4 m/s)	90	30	1. Low Temperature (LT): (−150 ± 10 °C) 2. Room Temperature (RT): (24 ± 5 °C) 3. High Temperature (HT): (135 ± 10 °C)	JSC −1A	25

2.3. Particle impact and deformation visualization

The high-velocity impact of erodent particles is achieved by using a sandblast gun with compressed air as propelling media (Fig. 1 C). The particles are propelled with compressed air at high pressures ranging from 0–0.8 MPa through the gun to obtain particle velocities up to 250 mph (112 m/s). A high-speed camera with up to a million FPS (frame per second) configuration is placed outside the viewports, with necessary ambient lighting of up to 50000 lumens for the visualization of erodent-propelled particles. For micro-in-situ impact capturing, a microscopic tube lens was used at a standoff distance of 1 cm away from the impact zone (Fig. 1D). Firstly, the propelled velocity from the nozzle is calculated by capturing the particles frame by frame. The distance traveled in frames/time in seconds gives the impact velocity.

$$Time\ in\ seconds = \frac{No.of\ frames\ particles\ travelled}{Frames\ per\ second} \tag{1}$$

$$Velocity\ of\ Particle = \frac{Distance\ particle\ travelled\ in\ amount\ of\ frames}{Time\ in\ seconds} \tag{2}$$

The distance between particles in subsequent frames is measured using the nozzle diameter as the scale to calculate the impact velocity. The high-speed camera is also used to visualize the in-situ particle deformation behavior during the impact. XCitex ProAnalyst motion analysis software (MA, USA) was used to track the particle trajectory, including approach, impact, and rebound. The velocity profile from the particle trajectory and tracking was used to calculate approach and rebound velocities for deformation analysis and energy balance calculations. A detailed explanation of velocity estimation and the computation of energy absorption is provided in Supplementary File, **Section 2**.

2.4. Test specimens and lunar erosion conditions

The three test specimens, including Ti6Al4V substrates, APS, and VPS coatings (Fig. 2A), were cut into square pieces of 1.4 cm × 1.4 cm size and ground down using 400-grit SiC paper at low polishing force for 5 min and 1200-grit SiC paper for 1 min to ensure the same surface integrity (inset Fig. 2 A). The erosion parameters (Table 2) were chosen to replicate the lunar erosion conditions as closely as possible.

Table 3
Mechanical properties of test specimens.

Specimen	Elastic Modulus (GPa)	Microhardness (HV)	Fracture Toughness (K_{IC} – MPa$\sqrt{M}$)
APS Ti/2 vol% hBN	94	925 ± 136	1.51
VPS Ti/2 vol% hBN	128	610 ± 54	13

This study chose two impact velocities, 50 mph (23 m/s) and a maximum possible 250 mph (112 m/s) by the compressed air capacity, to understand the material damage in low- and high-energy impact conditions. In 1971, Jaffe estimated a minimum velocity of 70 m/s for particles traveling 155 m from the Apollo 12 lander module (LM) to the Surveyor III probe[23]. Brownlee et al. (1972) suggested velocities of 300 m/s to 2000 m/s for particles accelerated by the LM [11]. Lane et al. (2008) projected velocities of 800 m/s to 1500 m/s near the lunar surface using computational fluid dynamics[24]. Since faster particles carry more momentum, examining the damage caused by slower particles (20–112 m/s), which are the highest speeds achieved in laboratory conditions, helps us understand the effects of lunar dust and micro-meteorite impacts. These slower particles mimic the lower-speed impacts of lunar dust and micro-meteorites, which are slower than larger meteoroids. This study provides insight into how lunar dust causes erosion, building a foundation for investigating impacts at higher speeds in the future. The primary focus of this work is to investigate the erosion resistance of the coatings under extreme lunar temperatures to ensure their multifunctionality. Based on previous literature[1–3,25] and experimental studies conducted in our lab, we have fixed the extreme testing conditions as an impact angle of 90 degrees and a duration of 30 s across three critical temperature regimes. An impact angle of 90º (normal to the substrate) is chosen to cover the maximum surface area on the substrate and to minimize any over-spray of regolith. The sandblasting gun was positioned 1 in. (~25 mm) away from the substrate, maintaining consistent flow to ensure the appropriate amount of simulant. After considering both the quantity of simulant and 200-µm coating thickness into consideration, a 30-second erosion duration was selected. The tests were conducted at three prominent lunar temperatures (−150, 25, and 150º C, respectively) to understand the effect of cryogenic and high temperatures on tested materials. The JSC-1A lunar mare regolith simulant (Fig. 2B) was chosen as erodent particles, considering the abrasive, sharp edges, and bi-modal size distribution (Fig. 2 C). The upcoming Artemis and Luna missions target the lunar mare as well as the poles. Hence, JSC-1A is an ideal simulant candidate to investigate the severe erosive impact of lunar dust.

Erosive wear was quantified using mass change, roughness changes from all specimens, and thickness loss for coating specimens. The mass change before and after erosion was measured using a precision weighing balance with 0.0001 g resolution. The roughness of the specimen before and after was measured using an optical profilometer (Nanovea, PS50, CA, USA) equipped with Scanning Probe Image Processor (SPIP) software. The top surface of specimens before and after testing and the cross-sectional coating area were characterized using SEM (JEOL-F100, Tokyo, Japan), with an accelerating voltage of 10 kV on gold-coated samples. The JSM-F100 uses a two-stage vacuum to reach 10^{-4} Pa. The SEM uses an In-lens Schottky plus field emission electron gun with a hybrid objective lens. The SEM consists of standard secondary and backscattered electron detectors with an integrated SMILE VIEW Lab software for image analysis. The thickness was measured using ImageJ analysis from cross-sectional SEM by averaging ten random images for each coating.

The fracture toughness (K_{IC}) of coatings was determined using the Anstis equation [26,27] for a radial-median crack system from a Vickers hardness indent using a load of 500gf.

$$K_{IC} = 0.016 \ \frac{F}{c^{3/2}} \ . \ \left(\frac{E}{HV}\right)^{1/2} \tag{3}$$

F, the applied load during the Vickers test (N); c, the crack length from the center of the indentation to the crack tip (m); E, Young's modulus (GPa); HV, the Vickers hardness (GPa). The elastic modulus of the coatings was obtained from an average of five random indentations using HIT300 (Anton Paar, USA).

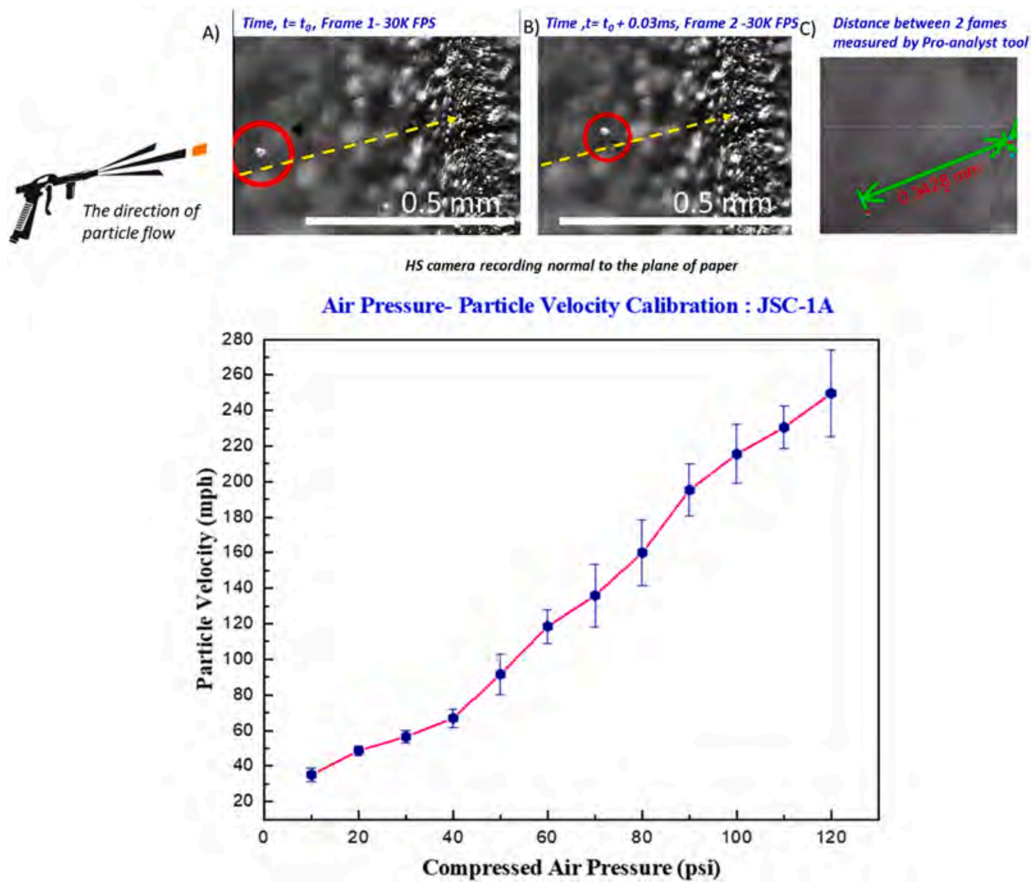

Fig. 3. (A-C) Snapshots from high-speed camera particle tracking used to calculate impact velocity and (D) Air-pressure-Impact Velocity calibration for JSC-1A.

3. Results and discussions

The Ti6Al4V substrate has a fracture toughness of 100 MPa$\sqrt{M}$ and a microhardness of 360 HV [28,29]. The microhardness of the substrate and coatings, along with their calculated fracture toughness, are listed in Table 3. Microhardness shows a threefold improvement for APS coatings, whereas VPS coatings indicate a twofold improvement compared to the pristine Ti6Al4V substrate. This is due to the formation of secondary phases such as TiO, TiB, and TiN during air plasma spray, which enhances the cumulative surface hardness of the coatings. A detailed description of phase formations and hardness response can be found in our previous publication[20].

Materials with higher fracture toughness resist crack propagation and are expected to withstand the applied impact energy without catastrophic failure. Here, the substrate and the VPS coatings are expected to withstand the applied impact forces by undergoing plastic

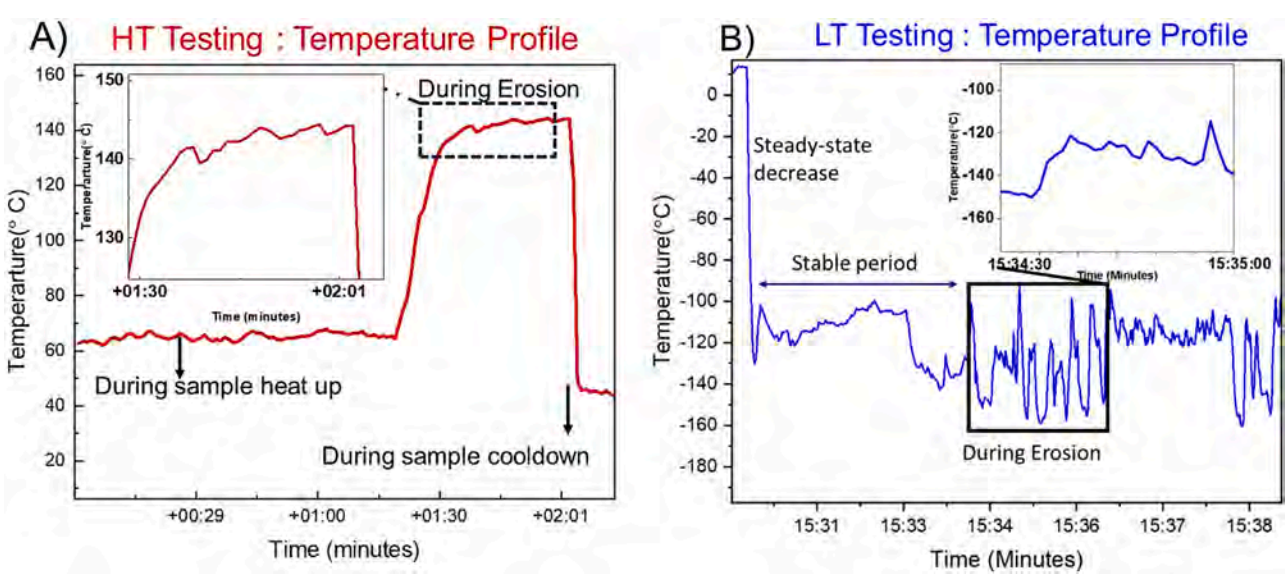

Fig. 4. Temperature profile during erosion for (A) high-temperature (B) low-temperature testing.

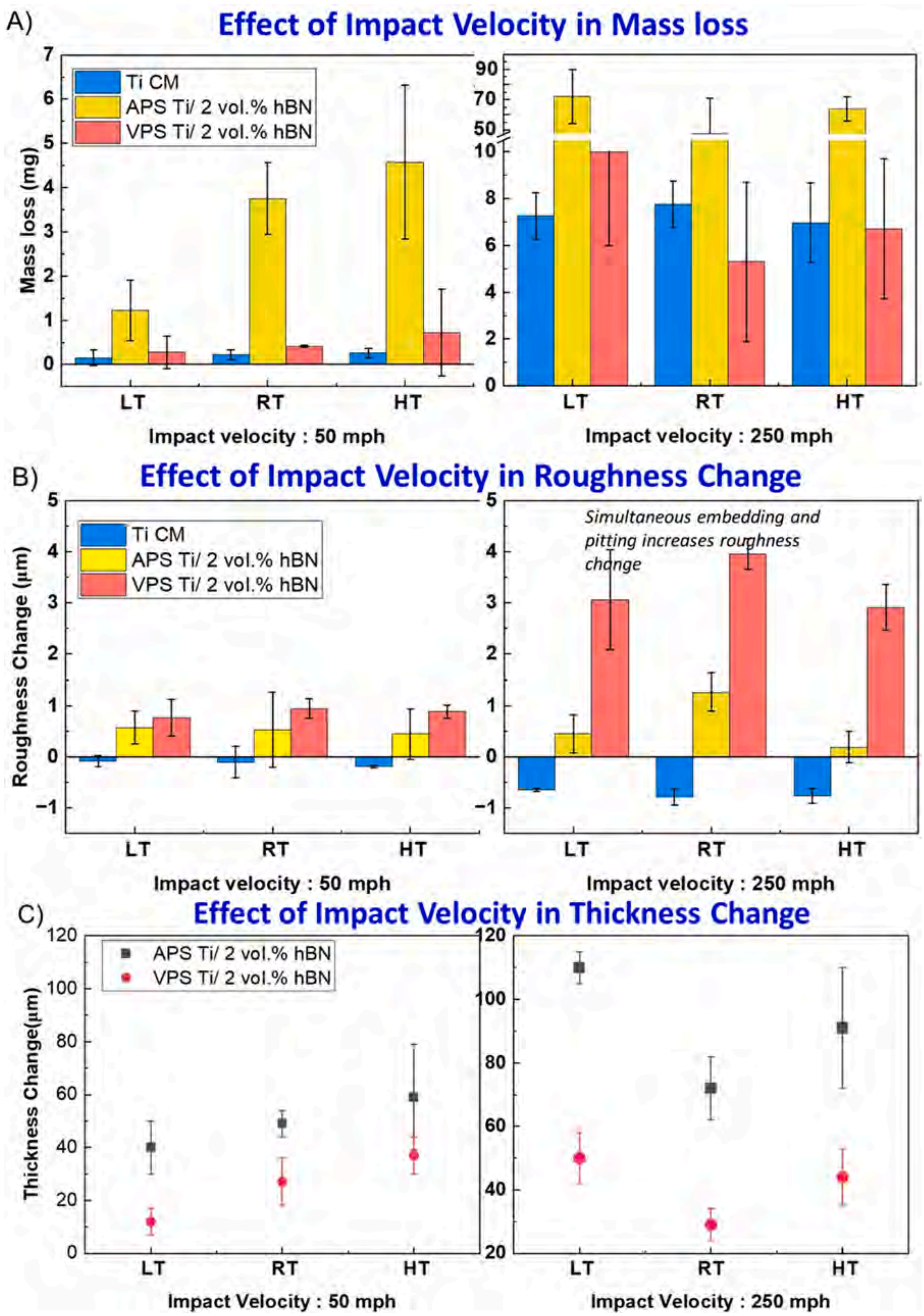

Fig. 5. Erosive wear quantification based on (A) Mass loss, (B)Roughness Change and (C) Thickness change recorded from erosion at a low impact velocity of 50 mph and high impact velocity of 250 mph.

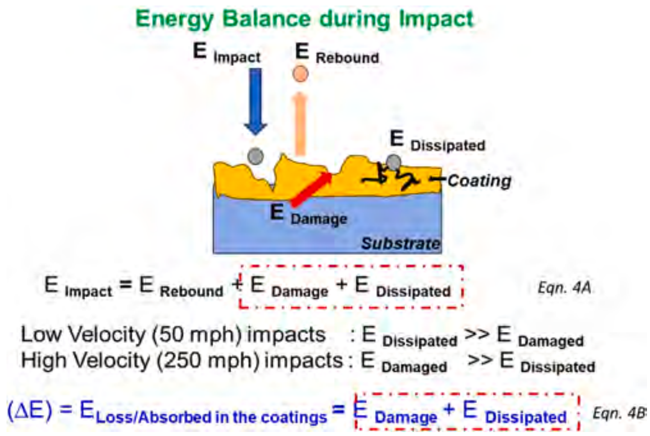

Fig. 6. Schematic representation of energy balance upon impact.

deformation from their high plasticity and fracture toughness, thereby resisting crack propagation. Due to their high brittleness and low fracture toughness of 1.51 MPa$\sqrt{M}$, APS coatings could initiate crack propagation and failure much faster than VPS coatings at the same impact energies, leading to poor erosive results.

3.1. Effect of impact velocity on erosion

The impact velocity of propelled particles using JSC-1A lunar regolith simulant using HS camera imaging (Fig. 3A-C) was calculated using Eqs. 1 and 2 for different compressed air pressure ranges from 0–0.8 MPa and shown in Fig. 3D. Particle size influences impact velocity with a standard deviation of 40 mph (18 m/s) observed at higher air pressures.

Different particle sizes lead to varying impact velocities due to the interplay of mass, surface area, and the applied forces or conditions. Smaller particles, with their lower mass and larger specific surface area, experience greater acceleration and higher velocities upon impact than larger particles. The maximum impact velocity possible with the current test setup of compressed air supply was found to be 250 ± 30 mph (112 ± 14 m/s). The temperature was monitored in situ during the erosion test using a K-type thermocouple-temperature control assembly. The temperature was kept constant at (140 ± 10 °C) for HT and (−150 ± 10 °C) for cryogenic conditions (Fig. 4 A and B). An initial time of 90 s was taken for the sample to heat, which increased to 5 min during cryogenic conditions to reach the steady state temperature up to −150 °C.

Slight variations in the order of ±10°C in temperature were observed during erosion, caused by the change in thermal gradient while particles hit the sample surface with high impact energies. This study quantifies erosive wear using mass loss, indicating material removal from the specimens, roughness change, and thickness change, especially for the coating materials. Fig. 5 A, B, and C represent mass loss, roughness change, and thickness change, respectively.

It is evident from Fig. 5A that heavy mass loss is observed at high velocity (250 mph) impacts due to the high impact energy created by the particles. The mass loss experiences a significant increase, with 13 times higher values for all samples recorded at high impact velocities compared to impacts at 50 mph. This increase is significantly larger in the case of LT (48 times for Ti CM, 59 times for APS, and 36 times for VPS, respectively) compared to RT and HT conditions. The high-velocity impacts possess high kinetic energy to exert a higher impact force with which particles strike the surface to remove more materials[30–32].

In addition, the impacting particles themselves undergo fracture and fragmentation, which create secondary abrasives, contributing to more material loss. The energy balance during impact can be represented by Eqn.4 A &B, in Fig. 6, where total impact energy is the sum of the energies of damage induced in the material, rebounded material, and the energy dissipated through the material by particle embedding [33]. For low-velocity impacts, the $E_{dissipated}$ by means of vibration, heat, and embedding by inelastic deformation is much larger than E_{damage} by global deformation affecting a larger area (Fig. 7B- high magnification SEM image), while local deformation on localized areas (Fig. 7B- low magnification SEM image), induces dominant E_{damage} in high-velocity impacts[33]. Hence, the material loss is much greater at high-velocity impacts for all materials. At 250 mph impact, APS coating suffers the most damage, notably in LT and HT conditions. The high brittleness and low fracture toughness of APS coatings result in inadequate absorption of impact force under cryogenic conditions, exacerbating the mechanical integrity and brittleness of the coating further (Fig. 7B). Hence, the coating suffers heavy mass loss as thickness loss upon impact.

Considering the energy balance upon impact of a larger particle (assuming spherical particle of ~ 400 μm diameter) on both the coatings (*based on velocity analysis from supplementary* video S3 & S4 *using pro-analyst tool*), it was observed that the particle, after impact, rebounds and travels 5 times the distance covered off APS coating compared to VPS coating. This indicates the magnitude of energy absorbed by the VPS coating is much higher than the APS coating, and the energy loss calculations *(Eqn.4 A and B)* in Table 4 indicate higher energy absorbed for VPS coatings compared to APS, assuming similar particle sizes. Detailed energy loss calculation for larger (>100 μm) and smaller-sized particles < 100 μm) at varying impact velocities is explained in Section 3.3.

The difference in energy loss may appear less pronounced in single particle impacts, but when considering cumulative energy loss from impacts involving particles of varying sizes, VPS coatings will exhibit a significantly greater absorbing enhancement compared to APS coatings due to their high fracture toughness, which enables them to withstand multi-particle impacts more effectively. For multi-particle impacts, energy loss (absorbed) can be found by (Eq.5),

$$\Delta E_{loss/abs} = \sum_{p=1}^{n} \frac{2}{3} \rho \pi r_p^{\,3} \left(V_i^{\,2} - V_r^{\,2} \right) \tag{5}$$

where $\rho -$ *particle density*, $r_p -$ *particle radius*, $V_i -$ *particle impact velocity*, $V_r -$ *particle rebound velocity*.

3.2. Effect of temperature on erosion

At LT, high-velocity impacts (KE of 4 $\times 10^{-04}$ for an average particle size of 45 μm) result in significant mass loss from the material surface, primarily due to enhanced sample brittleness that decreases the material's fracture toughness (in-situ supplementary video S2). This effect is more pronounced in APS coatings with a low fracture toughness (K_{Ic}) of 1.51 MPa$\sqrt{m}$, leading to a 51 % increase in mass loss, compared to substrate, while VPS coatings experience a 45 % increase in mass loss. At an impact speed of 50 mph, characterized by a low impact energy on the order of 3 × 10^{-08}, the enhanced hardness of materials at LT due to the cryogenic effect reduces mass loss significantly by 42 %, 67 %, and 61 % for Ti CM, APS, and VPS coatings, respectively, compared to RT. As the impact speed increases to 250 mph, VPS coatings outperform the substrate and APS coating with a 26 % and 6 % reduction in mass loss due to their plastic nature and high hardness compared to Ti CM substrates at RT and HT, respectively. In contrast, APS coatings suffer severe mass loss (514 % and 814 %) due to their poor fracture toughness and high brittleness in RT and High Temperature (HT) conditions.

It's worth highlighting the significance of time as a critical factor in erosion experiments. In this context, with a limited duration of only 30 s, the observed erosion enhancement in VPS coatings compared to the Ti substrate appears to be relatively modest, typically ranging from 15–30 %. However, this seemingly minimal difference becomes more pronounced over longer exposure times. In overextended durations, the Ti substrate tends to deteriorate rapidly under erosive conditions. In contrast, the VPS coatings demonstrate remarkable resilience by maintaining their

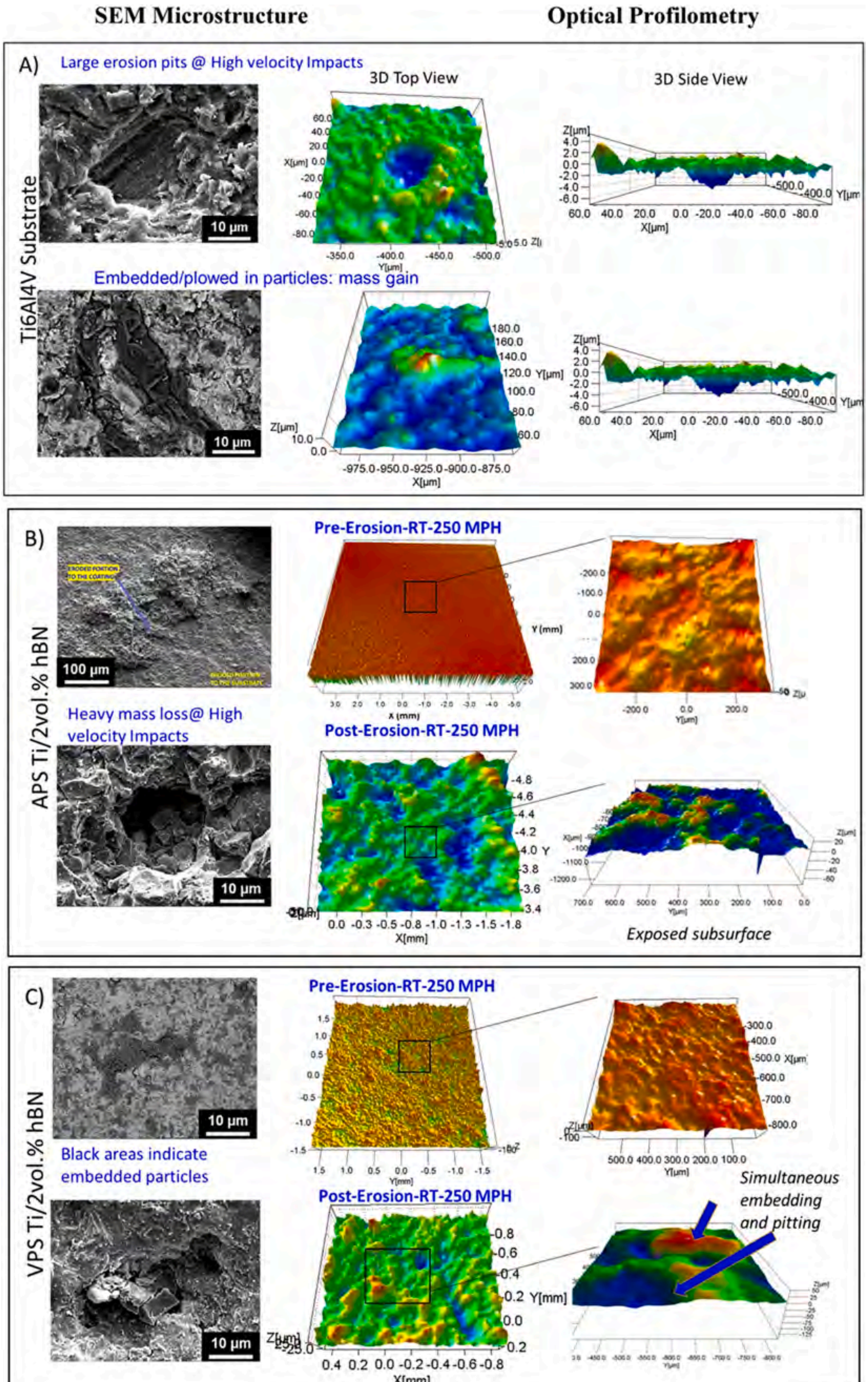

Fig. 7. SEM microstructure-optical profilometry correlation of materials at RT with 250 mph impact velocity (A) Ti6Al4V Substrate (B) APS Ti/2 vol% hBN coating (C) VPS Ti/2 vol% hBN coating.

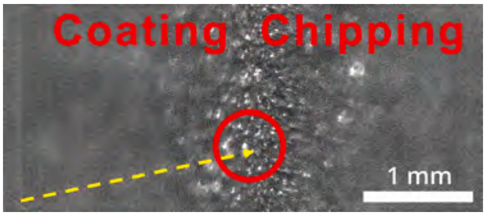

Video 3. The effect of a 250-mph impact on APS Ti/2 vol% hBN coatings, illustrating the chipping and failure of the coating. This video emphasizes the brittleness and reduced durability of the APS coating under extreme impact conditions.A video clip is available online. Supplementary material related to this article can be found online at doi:10.1016/j.triboint.2024.110339.

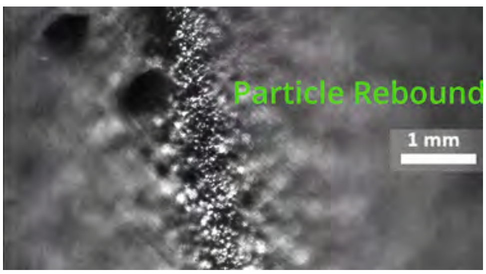

Video 4. A 250-mph impact test on VPS Ti/2 vol% hBN coatings showing particle rebound. This video captures the enhanced energy absorption and impact resistance of the VPS coatings, as particles bounce off the surface without significant damage.A video clip is available online. Supplementary material related to this article can be found online at doi:10.1016/j.triboint.2024.110339.

Table 4
Energy absorbed by the coating on a single particle (~ 400 μm diameter) impact.

Kinetic Energy particle impact at 250 mph (E_i) = 4.41 × 10^{-04} J		
Samples	**Rebound Kinetic Energy (J)**	**Energy loss /absorbed (E_{loss}) (J)**
APS Ti/2 hBN	4.33 × 10^{-06}	4.37 × 10^{-04}
VPS Ti/2 hBN	1.07 × 10^{-07}	4.41 × 10^{-04}

Video 2. A 250-mph impact test on the Ti substrate, where significant material loss is observed. The video showcases how the high-velocity impact results in severe erosion and damage to the uncoated Ti surface.A video clip is available online. Supplementary material related to this article can be found online at doi:10.1016/j.triboint.2024.110339.

structural integrity (in-situ *supplementary* video S1*: This Video shows the effect of erosion in longer durations of time at 50 mph, where VPS coatings exhibit high erosion resistance while Ti substrates rapidly degrade with high mass loss*). This emphasizes the importance of considering the temporal aspect in erosion studies to assess the performance and durability of protective coatings accurately. Mechanisms and features such as large erosion pits, plastic deformation, particle embedding, and plowing are observed in Ti substrates and VPS coatings (Fig. 7 A&C). Meanwhile, under these conditions, APS coatings exhibit crack formation, propagation, brittle fracture, and crater-like features (Fig. 7 B, Fig.S3 and S4). The thermal stresses induced at HT tend to initiate crack propagation in coatings during impact, leading to a 34 % and 26 % increase in mass loss for APS and VPS coatings, respectively, compared to RT under 250 mph impact velocity. The change in surface roughness is negative (Fig. 5B) for Ti substrates due to particle plowing and embedding due to its softer nature and high toughness (Fig. 7A, S3 and S4).

The roughness change for the Ti substrate is almost similar for LT and RT conditions at low-velocity impacts, and it increases by 90 % at HT conditions due to enhanced embedding of the particles by material softening (Supplementary image).

At high velocities, due to the higher volume of impacting particles and high kinetic energies, the roughness change increases by 3-fold in all temperature conditions for Ti substrates (Fig. 5B). The roughness change has a 6-fold increase in APS coatings compared to Ti substrates at LT due to high volume of material loss in the brittle condition at 50 mph and 1.5-fold rise in HT condition due to material softening and embedding. The roughness change is maximum at RT condition with 6-fold and 3-fold enhancement compared to Ti CM substrates at 50 and 250 mph, respectively (Fig. 5B). Both HT and LT have similar roughness trends for all three samples aided by heavy material loss at brittle conditions (LT) and particle embedding by material softening at high temperatures (HT). The highest roughness change is observed for VPS coatings since the coatings absorb impact energy by means of particle embedding, which shows a 10-fold increase at LT and RT and a 6-fold increase at HT in low velocities compared to the substrates. The roughness change increases by 6-fold at LT and RT and 5-fold at HT for 250 mph impacts (Fig. 5B). Fig. 8C shows the effect of particle embedding on the roughness profile from the profilometer images, where a severely embedded surface replaces a smooth surface pre-erosion. Corresponding in-situ HS camera snip shots and magnified SEM images, Fig. 8C shows the presence of sharp embedded particles on the coating surface (in-situ video S5, Fig.S3 and S4), which indicates the energy absorbance phenomenon.

Despite VPS coatings performing better in erosion resistance than Ti substrates and APS coatings, especially at higher impact speeds, Ti substrates still experience failure in extended periods of erosion due to plastic flow, deformation, and plowing (in-situ video S2, Fig.S3, and S4). This failure is mitigated by the higher hardness of VPS coatings, which protects them from fracture and failure by particle rebound due to its synergistic effect of optimum hardness and fracture toughness . Particle rebounding (Fig. 8C and in-situ video S4) is a significant phenomenon in VPS coatings, eliminating mass loss by energy absorption and thereby retaining the coating integrity even with high-velocity impacts.

3.3. Energy balance during impact: Synergistic effect of temperature, particle size, and velocity on erosion and impact energy absorption

Lunar erosion is a complex phenomenon involving various variables such as impact velocity, temperature, abrasive dust, and particle size of dust according to the interaction zones of structural materials with dust. It is necessary to develop materials (coatings) to counter the harsh environment developed by the synergistic effect of these variables and understand how it affects the total energy absorption of protective materials. In this study, a detailed analysis of particle-coating interaction with different particle sizes and temperatures was conducted at the varying impact velocities using in-situ high-speed camera particle capture and tracking.

Using the XCitex ProAnalyst motion analysis tool, the particle trajectory, including approach, impact, and rebound, was captured frame by frame (Example: Fig. 8A and B). The software's further data curation provides the velocity profile from the particle trajectory and tracking to calculate rebound velocity (Fig. 8C and D) and coefficient of restitution (Fig. 8E), where

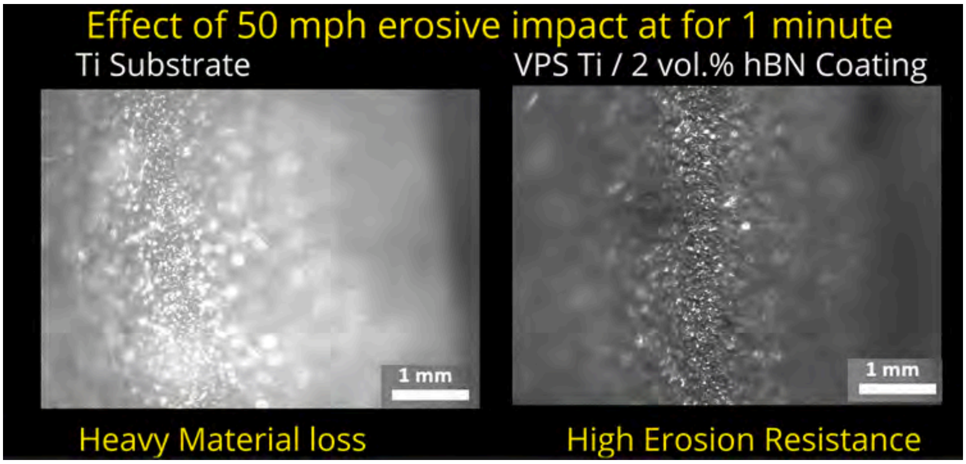

Video 1. A comparative analysis of the impact behavior between the Ti substrate and VPS coatings at 50 mph. This video highlights the superior performance of the VPS coatings, showing less material deformation and wear compared to the bare Ti substrate.A video clip is available online. Supplementary material related to this article can be found online at doi:10.1016/j.triboint.2024.110339.

$$\textit{Coefficient of Restitution} = \frac{\textit{Rebound velocity of particle}}{\textit{Impact Velocity of particle}} \quad (6)$$

and energy loss on impact (Eq.5).

Fig. 8 A and B schematically represent the particle trajectory of a big particle (> 100 µm) and small particle (<100 µm) on APS coatings at 50 mph (23 m/s) average impact velocity at RT (supplementary fig. S5). The green dotted line indicates the particle trajectory before and during, and the red dotted line indicates after impact. The analysis was conducted on both APS and VPS coatings at all temperature conditions and impact velocities for big and small particle sizes. Fig. 8 C and D (Fig.S3 and S4) represent the velocity change during impact at 50 mph and 250 mph at RT conditions. Both the impact and rebound velocities are much higher for smaller particles, considering small particles travel further (i_L and r_L are higher for smaller particles, and the travel time is lower Fig. 8A &B) for the same velocity. It is evident from the plot that the rebound velocity is much higher for the APS coatings compared to the VPS coatings, indicating a higher velocity change ΔV for VPS coatings at both velocities and particle sizes as,

$\Delta \boldsymbol{V}_{\boldsymbol{VPS\text{-}B}} > \Delta \boldsymbol{V}_{\boldsymbol{APS\text{-}B}}$: $\Delta \boldsymbol{V}_{\boldsymbol{VPS\text{-}S}} > \Delta \boldsymbol{V}_{\boldsymbol{APS\text{-}S}}$: *S- Smaller particles and B-Bigger particles*

At RT and 50 mph, the $\Delta V_{VPS\text{-}S}$ and $\Delta V_{VPS\text{-}B}$ are 38 % and 107 % higher than the $\Delta V_{APS\text{-}S}$ and $\Delta V_{APS\text{-}B}$, respectively (Fig. 8C). Similarly, at 250mph, this increase is 8 % and 33 %, respectively, and a similar trend is observed at LT and HT conditions as well. The higher velocity change is responsible for higher energy absorption by the coating by transferring impact energy to energy dissipation, as per equation 4. Fig. 8E represents the plot of the coefficient of restitution (COR) of both coatings against all tested conditions. It is evident that the impact of VPS coatings under all conditions almost remains under the inelastic range. Considering the ductile nature of VPS coatings and higher fracture toughness, the coating tends to absorb higher energy during impact, resulting in a high-velocity reduction of the impacting object (in-situ video S4). This energy loss can be in the form of heat, plastic deformation of the material, and embedding/plowing, as seen from the post-erosion microstructure-profilometry images in Fig. 8C (in-situ video S5). On the contrary, APS coatings at lower impact velocities show a coefficient of restitution in the elastic ranges, especially at RT and HT, indicating a low net energy transfer resulting in higher rebound velocities.

The CORs of APS coatings are also seen to be always higher compared to VPS coatings under all impacting conditions for smaller and bigger particle sizes. The coefficient of restitution (COR) decreases with increasing impact velocity due to the higher energy dissipation during the collision. At higher impact velocities, materials experience greater deformation, both elastic and plastic, which leads to more energy being absorbed rather than being restored during the rebound. Additionally, increased impact may cause microfractures and other forms of damage (Fig. 9), further reducing the rebound velocity and restitution as more energy is lost to permanent deformation and heat. This has been addressed in the revised manuscript for clarity. The high CORs in the RT and HT condition for APS coatings indicate a low net impact energy transfer to the coatings. The coatings fail to absorb the higher impact energies generated by the particles compared to VPS for the same conditions, hence resulting in a fracture and fragmentation, thereby incurring heavy mass loss (in-situ video S3).

The energy balance calculation (Eq.5) based on rebound velocity tracking from coatings at various impact velocities and particle sizes are shown in Fig. 9A and B. Corresponding images from Fig. 9C to F shows an example of cross-sectional thickness loss from SEM micrographs indicating how coatings fare against the high impact energies. In comparison of Fig. 9A and B, it is obvious that a higher energy transfer (~two orders of magnitude) is occurring at higher impact velocities of 250 mph compared to 50 mph due to the higher average velocity of impacting particles. Another striking observation is that both plots follow the inverse trend of mass loss plots, indicating that mass loss and energy absorption by the coatings are inversely proportional. As the coatings absorb higher energy during impact, the mass loss from the surface is reduced by energy dissipation through mechanisms such as plastic deformation and embedding, which are prominently observed in VPS coatings. As energy loss reduces, fracture and fragmentation by E_{damage} preceded over energy dissipation, resulting in a higher mass loss. Overall, for both velocities and particle sizes, the energy loss/absorbed can be represented as,

$\Delta V_{VPS\text{-}B} > \Delta V_{APS\text{-}B} > \Delta V_{VPS\text{-}S} > \Delta V_{APS\text{-}S}$

At 50 mph and LT, the energy loss for bigger and smaller particles between APS and VPS coatings is almost similar, with VPS coatings having a slightly higher energy absorbance than APS coatings.

The impact energy generated by the particles at low velocity is insufficient to generate mass loss from the materials since the material gets harder at low temperatures, as schematically represented in Fig. 10. At 250 mph, the high kinetic energy of impacting particles induces heavy mass loss from the brittle coating surface (Fig. 10). The impact energy absorbed by the VPS coatings is higher by 8 % and 2 % for

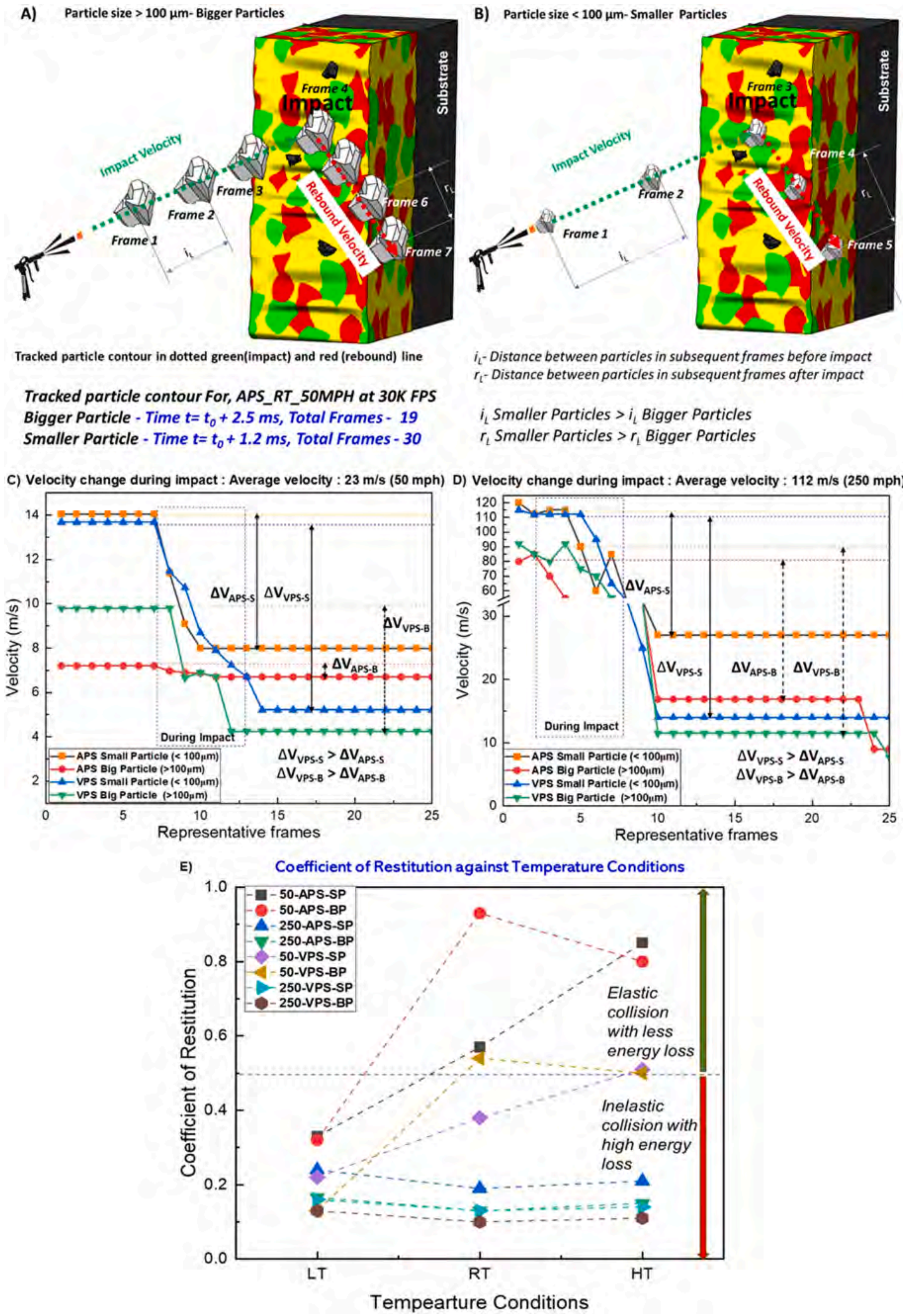

Fig. 8. Schematic representation of High-speed camera – Pro analyst analysis of particle tracking on the APS coatings at RT at 50 mph (A) Big particles (B->100 µm); (B) small particles (s-<100 µm) Representation of velocity change before-during-after impact for APS and VPS coatings at RT (C) at 50 mph (D) at 250 mph; (E) Coefficient of restitution of small and large particles on APS and VPS coatings at all temperatures(LT, RT and HT) and velocities.

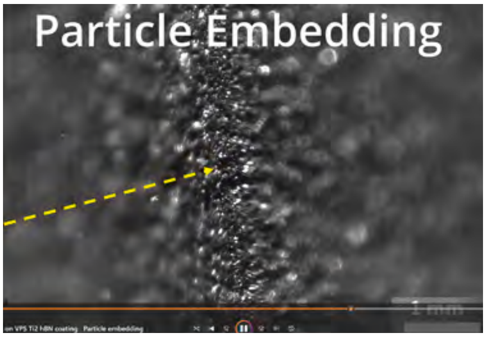

Video 5. A close-up of the 250-mph impact on VPS Ti/2 vol% hBN coatings, demonstrating particle embedding. This still provides insight into the coating's capacity to absorb energy and trap particles, enhancing erosion resistance compared to the uncoated substrate or APS coatings.A video clip is available online. Supplementary material related to this article can be found online at doi:10.1016/j.triboint.2024.110339.

smaller and bigger particle sizes, respectively, compared to APS coatings (Fig. 9 B). Hence, VPS has a reduction in mass loss compared to APS. At RT, the mass loss is higher than LT, while VPS coatings have higher energy absorbed for particle sizes and impact velocities. At 50 mph, the E_{abs} is 8 % and 5 % higher for smaller and bigger particles in VPS compared to APS coatings. Similarly, at 250 mph, this enhancement is 3 % and 2 % higher, respectively. The low-velocity impacts induce slight mass loss from coating material by plowing or embedding (Fig. 10), while VPS coating outperforms both the Ti substrate and APS coatings. At higher velocities, particles impacting normal to the surface embed under high impact forces, creating crack formation and propagation, causing fracture. Large erosion pits and craters are found in both normal and angular impacts (Fig. 8B). The smaller sharp-edged particles plow into the coating surface, initiating chipping from the APS surface. In contrast, VPS coating absorbs this impact energy through plastic deformation and embedding (Fig. 8B &C, in-situ Video S4 and S5). The cross-sectional SEM micrographs of coatings from Fig. 10C-F indicates slight chipping/material loss from the VPS coatings, which entirely remain intact and maintain their structural integrity. In contrast, APS coatings suffer a severe mass loss due to the heavy impact of particles at 250 mph and show severe chipping and material loss at 50 mph. At HT, the energy absorbance increases by 4 % for VPS coatings at both velocities for bigger particles since the material gets softer by plastic flow due to high temperatures (Fig. 10). For smaller particles, this enhancement is 6 % for 50 mph, and 3 % for 250 mph. The cross-sectional SEM micrographs indicate the same trends as in RT for all temperature conditions (Fig. 9 C-F). VPS coatings remain fully intact with minor material loss, while APS coatings suffer severe material loss and delamination due to impacting particles due to their insufficient impact energy absorption. The SEM images of the top surface in (Fig. 9 G-J) also correspond to this analysis. At 50 mph, the APS top surface shows splat disintegration, large erosion pits, and microcracks in the coating surface. In contrast, VPS coatings indicate a densified splat with no visible damage across the surface (Fig. 9 G and H). Also, hBN particles with an average size of 1–5 μm were utilized in this study, which, as supported by literature, have been shown to enhance the cohesive strength between splats during plasma spraying. This is mainly due to the improved wettability of the hBN particles, leading to stronger bonding at the inter-splat interfaces and reducing the likelihood of delamination during erosion[34–36]. This behavior is evident from the greater inter-splat delamination observed in APS coatings with lower hBN retention (~0.5 wt%) compared to VPS coatings, which exhibited higher hBN retention (~1 wt%) as determined by XRD Rietveld analysis, previously reported in our earlier work [20,21]. At a high velocity of 250 mph, heavy material loss is observed in APS coating, which exposes the underlying substrate. Large erosion pits, fracture, fragmentation, and microcracks contribute to the brittle fracture phenomenon in the coatings (Fig. 10 I and J). In contrast, VPS coatings absorb high-velocity impact, and fragments or remnants of impacting particles are seen to be embedded on the surface (Fig. 10J). Hence, it is evident from the velocity tracking and energy balance calculations that VPS coating has a higher energy absorbance upon impact due to its plastic nature and high fracture toughness, while APS coating suffers severe material loss due to its high brittleness. In our previous study, both APS and VPS Ti/2 vol% hBN coatings have demonstrated excellent abrasive wear resistance improvement of up to 90 % and neutron shielding improvement of up to 30 % [20]. In addition, the high erosion resistance observed in this study is a testimonial to the potential applicability of VPS Ti/2 vol% hBN coatings as a multifunctional protective coating to counteract the extreme abrasion, erosion, and radiation effects of the lunar environment.

3.4. Modified erosion index with fracture toughness and temperature

The inherent erosion performance of APS and VPS coatings, derived from comprehensive mass loss-energy balance analysis supported by SEM, profilometry, and high-speed camera imaging, can be visually depicted in Fig. 11.

Recalling the mechanical properties of the coatings from Table 3, it is observed that VPS coatings have a much higher fracture toughness of 13 MPa$\sqrt{M}$ compared to 1.521 MPa$\sqrt{M}$ of APS coatings. This is due to a higher percentage of secondary reaction products (TiO) in the atmospheric plasma spray process, which increases the cumulative hardness of coatings to make them brittle [20]. The vacuum spraying conditions help in the retention of higher percentages (≈ 70 %) of the inherent Ti phase (the yellow-colored region in Fig. 11), which retains its original plasticity in the deposited coatings [20]. Hence, during impact, APS coatings follow a brittle material erosion model, where particle impacts create radial and lateral cracking on the impacting surfaces, further creating fracture fragmentation and material loss from the surface[30, 32,37]. In contrast, with their high fracture toughness and retained plastic properties, VPS coatings reduce the mass loss and erosion rate by plastic deformation and embedding by cutting mechanism.

The proposed equation by Evans et al. [38] in 1978 for erosion volume loss by analyzing radial and lateral cracks and fracture threshold using impact dynamics for brittle materials was given by Eq.7,

$$\Delta Q \propto \frac{V_p^{19/6} \; r_p^{11/3} \rho_p^{1/4}}{K_t^{4/3} H_t^{1/4}} \tag{7}$$

Where V_p-impact velocity, r_p-particle radius, ρ_p-particle density, K_t-target material fracture toughness, H_t-target material hardness. Later, various studies and researchers came up with several relations to improve upon this model by incorporating the effect of depth of crack. [39], particle size[40]and area of crack formation based on the maximum stress criterion[41]. Nevertheless, these studies haven't incorporated the effect of ambient temperature on the target material and its influence on crack formation, propagation, and material loss of the erosion mechanism. Similarly, for ductile materials, Hutchings et al. [42] developed an erosion model caused by platelet formation at normal incidence based on the critical strain criterion and employing an energy-based approach. The resulting erosion equation reflects the influence of target material characteristics such as ρ_t- density, H_t -hardness and erosion ductility (Ω_c), and f_1-fraction of the volume of indentation, with assumptions made regarding the negligible effects of elastic forces and particle deformation during surface interaction, given by Eq.8,

$$\text{Total erosion rate,} \quad \varepsilon_m = 0.033 \frac{f_1 \quad \rho_t \quad V_p^3 \rho_p^{1/2}}{\Omega_c^2 H_t^{3/2}} \tag{8}$$

Even though Sundararajan and Shewmon [43] postulated an erosion model later based on lip formation considering heat capacity and

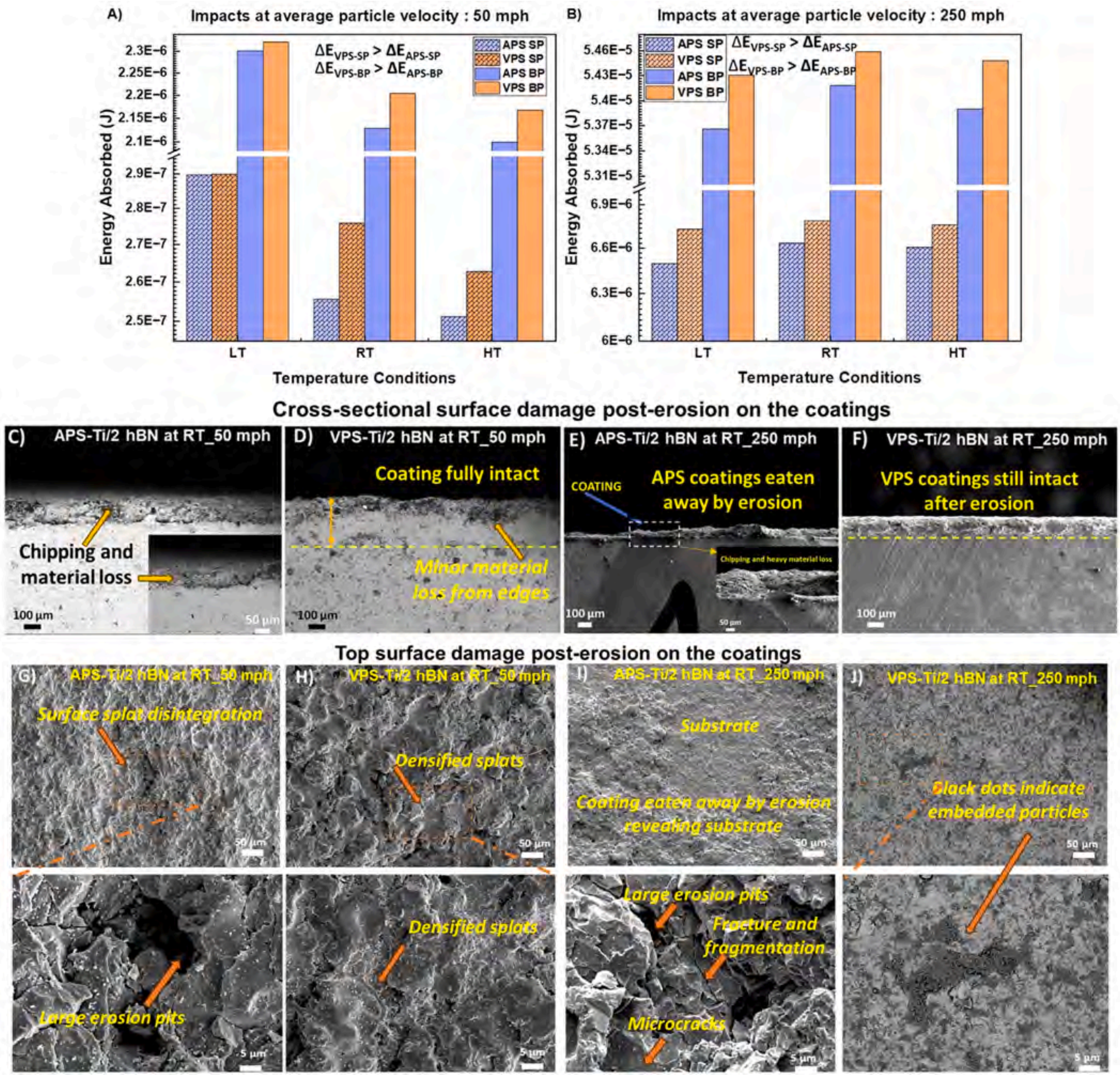

Fig. 9. Energy absorbed by the APS and VPS coatings at all temperatures (LT, RT, and HT) and velocities against the impact of small and large particles. (A) 50 mph (B) 250 mph; Thickness loss comparison of coatings at RT (C-D) 50 mph (E-F) 250 mph: Top surface damage post erosion of coatings at RT. (G-H) 50 mph (I-J) 250 mph.

melting temperature of the target materials, respectively, the influence of ambient temperature on the erosion effect on the target surface was neglected in the upcoming erosion models. In our review [3]of lunar regolith-induced abrasion and erosion on materials surface, we proposed an erosion index incorporating several parameters such as R-material part, or system risk to mission success, H-weighted average hardness value of localized mineralogy, I_v-Impact velocity of erosive particles, I_a-Impact angle at particle hits the sample surface, F-the frequency of dust particle interactions, T-Temperature at which material is exposed to abrasive conditions. Based on the current study, a modified erosion index is proposed incorporating the fracture toughness (K_{Ic}), time exposed to erosion (t), and ambient temperature (T_a) to which target materials are exposed. This will provide a more comprehensive understanding of erosion mechanisms, considering the influence of these crucial parameters on material response to erosive forces. This index can be represented in Eq.10 as,

$$Erosion\ Index = f\ (R,\ H,\ I_v,\ I_a\ F,\ K_{Ic},\ t,\ T_a) \tag{9}$$

Similarly, incorporating the fracture toughness (K_{Ic}), time exposed to erosion (t), ambient temperature (T_a), and particle sphericity to accommodate randomness in shapes(Ψ) as variables in the classical brittle and ductile material models, Eq.7 and Eq. 8 can be modified as

$$\text{For brittle materials, } Total\ volume\ loss\Delta Q \propto \frac{V_p^{\frac{19}{6}}\ r_p^{\frac{11}{3}}\rho_p^{\frac{1}{4}}}{K_t^{\frac{4}{3}}H_t^{\frac{1}{4}}}.T_a^{\ n}.t.\Psi \tag{10}$$

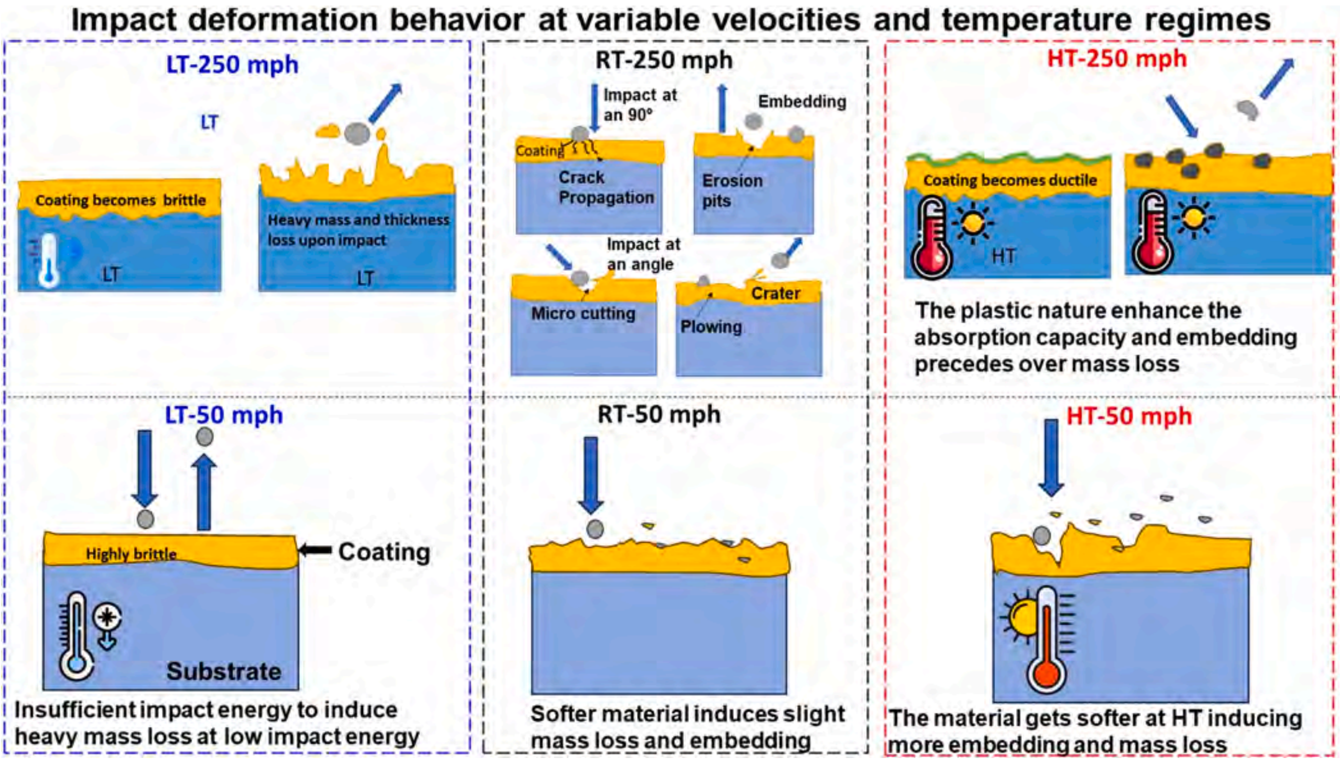

Fig. 10. Schematic representation of impact-deformation behavior of coatings against variable velocities and temperature conditions.

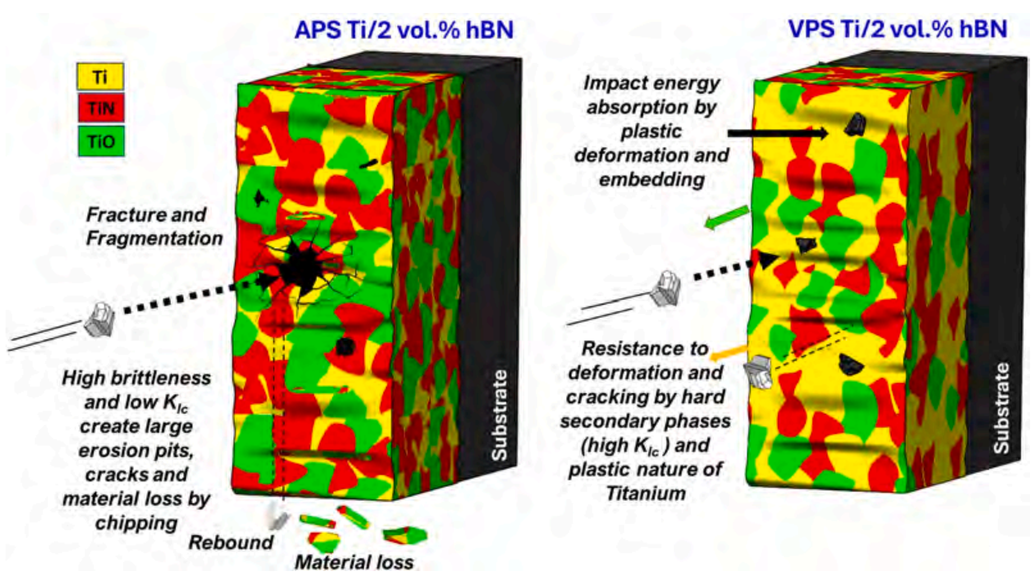

Fig. 11. Schematic representation of erosion effect overview on APS and VPS coatings.

$$\text{For ductile materials}, \textit{Total volume loss}, \ \Delta Q \propto 0.033 \frac{f_1 \ \rho_t \ V_p{}^3 \rho_p{}^{\frac{1}{2}}}{\Omega_c{}^2 H_t^{\frac{3}{2}}} . T_a{}^n . t . \Psi \quad (11)$$

Where n- power law exponent of ambient temperature.

While these erosion theories outlined are based on support from previous erosion data, their functional reliance on material properties varies considerably. The models presented (Eqs. 10 and 11) for total volume loss in brittle and ductile materials are expressed as semi-quantitative temperature and erosion time functions, integrating principles from classical fracture mechanics. These models account for critical factors such as impact velocity (Vp), particle radius (rp), and material properties like fracture toughness (Kt) and hardness (Ht). However, due to the inherent variability in the distribution of impact velocities across different particle sizes in the erodent, the equations have limitations in fully capturing erosion behavior over a wide range of temperature conditions. This issue is compounded by the data set, which includes only three temperature regimes (−150C, RT, and 135 C), making it challenging to develop a robust predictive model. To improve the accuracy and applicability of this model, future studies should focus on expanding the temperature range and exposure times to capture the influence of temperature on erosion mechanisms. Additionally, using a wider variety of erodents with different sizes, shapes, and densities will address the randomness in particle characteristics and their effect on volume loss. Finally, systematically varying the impact velocity will refine the model's predictive capabilities, ensuring a more accurate reflection of the relationship between kinetic conditions and material erosion. Moving forward, these models could be developed into fully quantitative equations by integrating machine learning, accounting for a broader range of particle morphologies, sizes, and temperature conditions, improving predictive accuracy and generalization. These efforts will contribute to a more comprehensive validation and refinement of the model for predicting erosion in both brittle and ductile materials under diverse thermal and impact conditions.

4. Conclusions

The lunar erosion performance of novel Ti/2vol% hBN multifunctional coatings was evaluated using a custom-made planetary erosion test rig to simulate extreme lunar conditions. This study emphasizes the outstanding erosion resistance of VPS Ti/2 vol% hBN coatings, which strike an ideal balance between hardness and flexibility, significantly reducing mass and thickness loss under varying temperature conditions. In contrast, the inherent brittleness in APS coatings leads to severe material loss under high and low-impact velocities, with significant mass loss observed, particularly at 250 mph. APS coating suffers severe mass loss in all conditions, while 31 % and 5 % reductions in mass loss are observed for VPS coatings due to their plastic nature and high hardness compared to Ti substrates at RT and HT conditions, respectively.

At lower impact velocities (50 mph), the trend in mass loss is influenced by the hardness of materials across different temperature conditions. While Ti substrates suffer failure after prolonged erosion periods, the VPS coatings effectively safeguard against fracture and failure across all temperature conditions. The study highlights the critical role of ambient temperature on erosion mechanisms. Low temperatures increase brittleness and mass loss, while high temperatures cause plastic flow and particle embedding. Despite these variations, VPS coatings are more resilient than Ti substrates and APS coatings. Using SEM, optical profilometry, and high-speed imaging, fundamental erosion mechanisms like particle embedding, pitting, and rebounding were evidenced. Analysis of rebound velocity, coefficient of restitution, and energy balance confirms the superior energy absorption of VPS coatings, resulting in lower mass loss and better material protection than APS coatings. Moreover, the study proposes a modified erosion index and erosion models incorporating fracture toughness, time exposed to erosion, particle sphericity and ambient temperature, providing a comprehensive framework for quantifying erosion resistance. The study's findings highlight the superior erosion and the abrasion and radiation resistance of Ti-BN coatings, making them highly promising candidates for durable aerospace coatings in extreme lunar environments.

CRediT authorship contribution statement

Michael Renfro: Validation, Methodology, Investigation, Data curation. **William Scott:** Writing – review & editing, Investigation. **Cheol Park:** Writing – review & editing, Validation, Supervision, Methodology, Investigation, Data curation. **Sang-Hyon Chu:** Writing – review & editing, Validation, Investigation, Data curation. **Sara Rengifo:** Supervision, Resources, Project administration, Methodology, Investigation, Funding acquisition. **Abhijith Kunneparambil Sukumaran:** Writing – original draft, Visualization, Validation, Formal analysis, Data curation, Conceptualization. **Sohail M.A.K Mohammed:** Methodology, Investigation. **Brandon Aguiar:** Methodology, Investigation. **Arvind Agarwal:** Writing – review & editing, Supervision, Project administration, Methodology, Investigation, Funding acquisition, Data curation, Conceptualization.

Declaration of Competing Interest

The authors declare that they have no known competing financial interests or personal relationships that could have appeared to influence the work reported in this paper.

Acknowledgments

The authors gratefully acknowledge support from the National Aeronautics and Space Administration (NASA) through the 80MSFC21P0018 grant. The usage of facilities at the Advanced Materials Engineering Research Institute (AMERI) is recognized for the research reported in this study.

Statement of originality

This manuscript has not been published previously by any of the authors and is not under consideration for publication in another journal at the time of submission. All authors have seen the manuscript and approved to submit to your journal.

Appendix A. Supporting information

Supplementary data associated with this article can be found in the online version at doi:10.1016/j.triboint.2024.110339.

Data availability

Data will be made available on request.

References

[1] Clegg, R.N., Metzger, P.T., Huff, S., & Roberson, L.B. (2011). Lunar Soil Erosion Physics for Landing Rockets on the Moon. In Lunar and Planetary Science Conference (No. 1608, p. 1450).
[2] Land N.S., Schozz H.F. Scaled Lunar Module Jet Erosion Experiments N A S A TN D-505 1.
[3] Kunneparambil Sukumaran A, Zhang C, Nisar A, Agarwal A. Recent trends in tribological performance of aerospace materials in lunar regolith environment – a critical review. Adv Space Res 2024;73:846–69. https://doi.org/10.1016/j.asr.2023.10.039.
[4] Metzger P., Lane J.E., Immer C., Gamsky J., Hauslein W., Li X., et al. Scaling of Erosion Rate in Subsonic Jet Experiments and Apollo Lunar Module Landings. 2010. ⟨https://api.semanticscholar.org/CorpusID:131482319⟩.
[5] Sukumaran AK, Zhang C, Nisar A, Rengifo S, Agarwal A. Tribological behavior of Al 6061 and Ti6Al4V alloys against lunar regolith simulants at extreme temperatures. Wear 2023:530–1. https://doi.org/10.1016/j.wear.2023.205028.
[6] Bühler CA. Experimental investigation of lunar dust impact wear. 244–51 Wear 2015:342–3. https://doi.org/10.1016/j.wear.2015.09.002.
[7] Marshall G.C., Schrader C.M., Rickman D.L., Mclemore C.A., Fikes J.C. Lunar Regolith Simulant User's Guide. 2010, NASA/TM—2010–216446.
[8] F.S., C.J.M. Johnson J.M. EDE, Carroll D.E. Evans Vacuum measurements on the lunar surface 1971 450 451.
[9] Williams JP, Paige DA, Greenhagen BT, Sefton-Nash E. The global surface temperatures of the moon as measured by the diviner lunar radiometer experiment. Icarus 2017;283:300–25. https://doi.org/10.1016/j.icarus.2016.08.012.
[10] Immer C, Metzger P, Hintze PE, Nick A, Horan R. Apollo 12 Lunar Module exhaust plume impingement on Lunar Surveyor III. Icarus 2011;211:1089–102. https://doi.org/10.1016/j.icarus.2010.11.013.
[11] D. Brownlee, W. Bucher, P. Hodge. Analysis of Surveyor 3 Material and Photographs Returned by Apollo12: Primary and Secondary Micrometeoroid Impact Rate on the Lunar Surface: A Direct Measurement, 1972.
[12] James R. Gaier, Gaier J.R. The effects of lunar dust on EVA systems during the Apollo missions. NASA/TM-2005–213610 2005.
[13] NASA's management of the Artemis missions. 2021, Report No. IG-22–003.
[14] Rover Wheels - NASA Mars, ⟨https://llis.nasa.gov/lesson/22401⟩, September 2016.
[15] Mpagazehe J.N., Street K.W., Delgado I.R. Erosive Wear Characterization of Materials for Lunar Construction. 2012, NASA/TM—2012–217706.
[16] Mpagazehe J.N., Street K.W., Delgado I.R. "Kicking Up Some Dust": An Experimental Investigation Relating Lunar Dust Erosive Wear to Solar Power Loss. 2013, NASA/TM—2013–218068.
[17] Mpagazehe J.N., SKW, Jr, DIR, H.C.F., I. Prediction of erosive wear by exhaust-blown lunar dust through experimentally-validated computational. Proceedings of the International Astronautical Congress, IAC 2014;8:5835–5838.

[18] Mpagazehe JN, Street KW, Delgado IR, Fred Higgs C. An experimental study of lunar dust erosive wear potential using the JSC-1AF lunar dust simulant. Wear 2014;316:79–91. https://doi.org/10.1016/j.wear.2014.04.018.
[19] Wittbrodt A.C., Metzger P.T. NASA USRP-Internship Final Report Material Damage from Impacts of Lunar Soil Particles Ejected by the Rocket Exhaust of Landing Spacecraft. 2008.
[20] Sukumaran AK, Zhang C, Rengifo S, Renfro M, Garino G, Scott W, et al. Tribological and radiation shielding response of novel titanium-boron nitride coatings for lunar structural components. Surf Coat Technol 2024;476. https://doi.org/10.1016/j.surfcoat.2023.130300.
[21] Sukumaran AK, Orikasa K, Rengifo S, Renfro M, Scott W, Gray A, et al. Wear and neutron shielding resilience of titanium-hexagonal boron nitride coatings against extreme lunar radiation and thermal cycles. Surf Coat Technol 2024;492. https://doi.org/10.1016/j.surfcoat.2024.131185.
[22] Bacca N, Zhang C, Paul T, Sukumaran AK, John D, Rengifo S, et al. Tribological and neutron radiation properties of boron nitride nanotubes reinforced titanium composites under lunar environment. J Mater Res 2022. https://doi.org/10.1557/s43578-022-00708-w.
[23] Reports Blowing of Lunar Soil by Apollo 12: Surveyor 3 Evidence 26 Feb 1971, Vol 171, Issue 3973, pp. 798–799, DOI: 10.1126/science.171.3973.798.
[24] Lane J.E., Metzger P.T., Immer C.D. Lagrangian Trajectory Modeling of Lunar Dust Particles. doi.org/10.48550/arXiv.2305.19993.
[25] Metzger P, Lane JE, Immer C, Gamsky J, Hauslein W, Li X, et al. Scaling of erosion rate in subsonic jet experiments and apollo lunar module landings. March 2010, DOI: 10.1061/41096(366)21 Proc Earth Space 2010. March 2010, DOI: 10.1061/41096(366)21.
[26] Anstis GR, Chantikul P, Lawn BR, Marshall DB. A critical evaluation of indentation techniques for measuring fracture toughness. J Am Ceram Soc 1981. https://doi.org/10.1111/j.1151-2916.1981.tb10320.x.
[27] Nastic A, Merati A, Bielawski M, Bolduc M, Fakolujo O, Nganbe M. Instrumented and vickers indentation for the characterization of stiffness, hardness and toughness of zirconia toughened Al2O3 and SiC armor. J Mater Sci Technol 2015; 31:773–83. https://doi.org/10.1016/j.jmst.2015.06.005.
[28] Destefani JD. Introduction to Titanium and Titanium Alloys. Properties and Selection: Nonferrous Alloys and Special-Purpose Materials. ASM International; 1990. p. 586–91. https://doi.org/10.31399/asm.hb.v02.a0001080.
[29] Properties and Selection: Nonferrous Alloys and Special-Purpose Materials. ASM International; 1990. https://doi.org/10.31399/asm.hb.v02.9781627081627.
[30] Ruff A.W., Wiederhorn S.M. Erosion by solid particle impact. Gaithersburg, MD: 1979. https://doi.org/10.6028/NBS.IR.78–1575.
[31] Alqallaf J, Ali N, Teixeira JA, Addali A. Solid particle erosion behaviour and protective coatings for gas turbine compressor blades-A review. Processes 2020;8. https://doi.org/10.3390/PR8080984.
[32] Tarodiya R, Levy A. Surface erosion due to particle-surface interactions - a review. Powder Technol 2021;387:527–59. https://doi.org/10.1016/j.powtec.2021.04.055.
[33] Othman R, Ogi K, Yashiro S. Characterization of microscopic damage due to low-velocity and high-velocity impact in CFRP with toughened interlayers. 16-00151-16–00151 Mech Eng J 2016;3. https://doi.org/10.1299/mej.16-00151.
[34] Honglin M, Haichao Z, Honggang T, Guozheng M, Ming L, Haidou W, et al. Effects of hBN content and particle size on microstructure, mechanical and tribological properties of NiCr-Cr3C2-hBN coatings. Surf Coat Technol 2024;478. https://doi.org/10.1016/j.surfcoat.2023.130330.
[35] Saji VS. 2D hexagonal boron nitride (h-BN) nanosheets in protective coatings: a literature review. Heliyon 2023;9. https://doi.org/10.1016/j.heliyon.2023.e19362.
[36] Du L, Zhang W, Liu W, Zhang J. Preparation and characterization of plasma sprayed Ni3Al-hBN composite coating. Surf Coat Technol 2010;205:2419–24. https://doi.org/10.1016/j.surfcoat.2010.09.036.
[37] Yabuki A, Matsumura M. Theoretical equation of the critical impact velocity in solid particles impact erosion. Wear 233–235 1999:476–83.
[38] Evans AG, Gulden ME, Rosenblatts M. Impact damage in brittle materials in the elastic-plastic response regime. Proc R Soc Lond Ser A 1978.
[39] Wiederhorn SM, Lawn BR. Strength degradation of glass resulting from impact with spheres. J Am Ceram Soc 1977;60:451–8. https://doi.org/10.1111/j.1151-2916.1977.tb15531.x.
[40] Routbort JL, Scattergood RO, Kay EW. Erosion of silicon single crystals. J Am Ceram Soc 1980;63:635–40. https://doi.org/10.1111/j.1151-2916.1980.tb09851.x.
[41] Wang ZT. Erosion model for brittle materials under low-speed impacts. J Tribol 2020;142. https://doi.org/10.1115/1.4046019.
[42] Hutchings IM. A model for the erosion of metals by spherical particles at normal incidence. Wear 1981;70(3):269–81. https://doi.org/10.1016/0043-1648(81)90347-1.
[43] Sundararajan G, Shewmon PG. A new model for the erosion of metals at normal incidence. Wear 1983;84:237–58. https://doi.org/10.1016/0043-1648(83)90266-1.

Lunar Erosion Performance of Novel Ti-BN Multifunctional Coatings in a Custom-made Erosion Test Rig at Extreme Temperatures

Abhijith Kunneparambil Sukumaran[1], Sara Rengifo[2], Brandon Aguiar[1], Sohail M.A.K Mohammed[1], William Scott[2], Michael Renfro[3], Sang-Hyon Chu[4], Cheol Park[4] and Arvind Agarwal[1]

[1]Plasma Forming Laboratory, Florida International University, Miami, FL

[2]National Aeronautics and Space Administration, Marshall Space Flight Centre, Huntsville, AL,

[3] Plasma Processes, Huntsville, AL

[4] Advanced Materials and Processing Branch, NASA Langley Research Center, Hampton, VA

1.1 Composite Powder Preparation and Coating Synthesis

Composite Ti-hBN powder for plasma spray was prepared by mixing hBN powder (Fig. 1A, average particle size of 5 µm, surface area = 7.5 m²/g, density = 2.1 g/cm³) with Ti6Al4V powder (Fig. 1B, average size <30 µm, density = 4.5 m²/g) at concentrations of Ti6Al4V/2 vol% hBN and Ti6Al4V/10 vol% hBN.

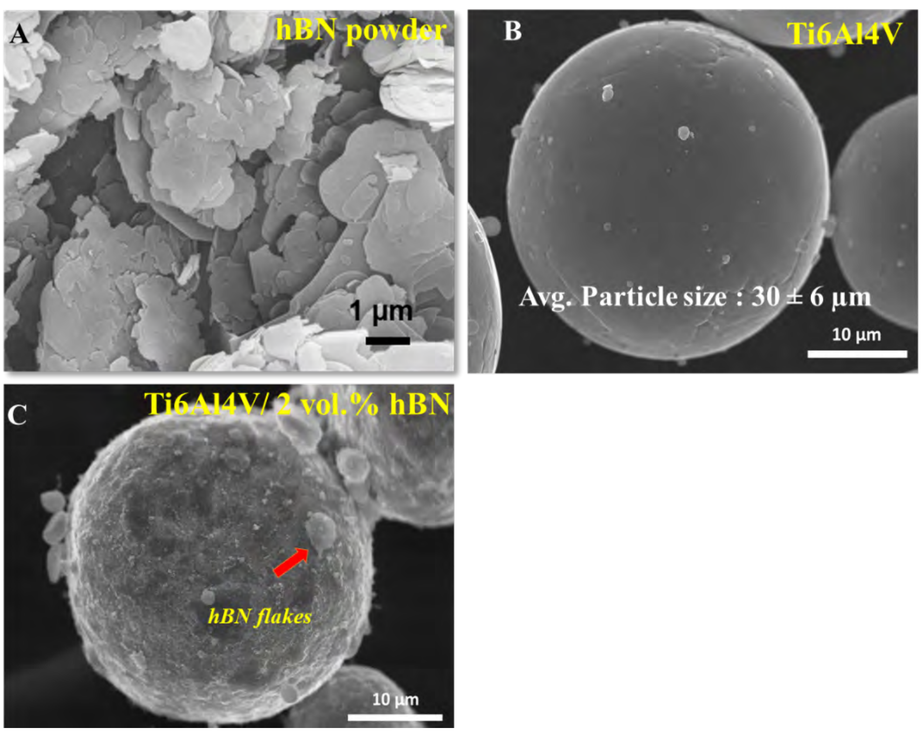

Figure S1: SEM images of (A) as-received hBN powder, (B) as-received Ti6Al4V powder, (C) Cryo-milled Ti6Al4V/2 vol.% hBN powder with well dispersed hBN flakes on Ti6Al4V powder, and the powder feed rate into the plasma plume decreases from B-C from 28 g/min to 22 g/min respectively.

Cryo-milling was employed using two grinding bowls (250 ml), and a mix of grinding balls (diameters: 0.51 cm and 1.91 cm) with a ball mass (MB) to powder mass (MP) ratio of 10. To ensure uniform mixing and preserve the spherical morphology of metal particles, the pre-mixing occurred in an argon-filled glove box (<58 ppm O_2). Additionally, to prevent oxidation, minimize metal particle deformation and heat generation, and promote hBN dispersion, the entire set was cooled to -97°C in liquid nitrogen before cryo-milling for 15 minutes. The resulting powders were sieved through a No. 30 sieve (600 µm mesh size) to remove grits. For coating deposition using atmospheric plasma spray (APS) and vacuum plasma spray (VPS), conventionally manufactured (CM) Al6061 and Ti6Al4V circular pucks (Φ 3.81 × t 0.64 cm) served as substrates. Substrates were cleaned with acetone and sandblasted with 54-grit alumina at 40 psi for 5 minutes to ensure proper surface roughness and integrity for coating adhesion. Before powder feeding, substrates were preheated with one pass of the plasma plume to minimize the coefficient of thermal expansion (CTE) mismatch and prevent thermal stresses, cracks, and delamination.

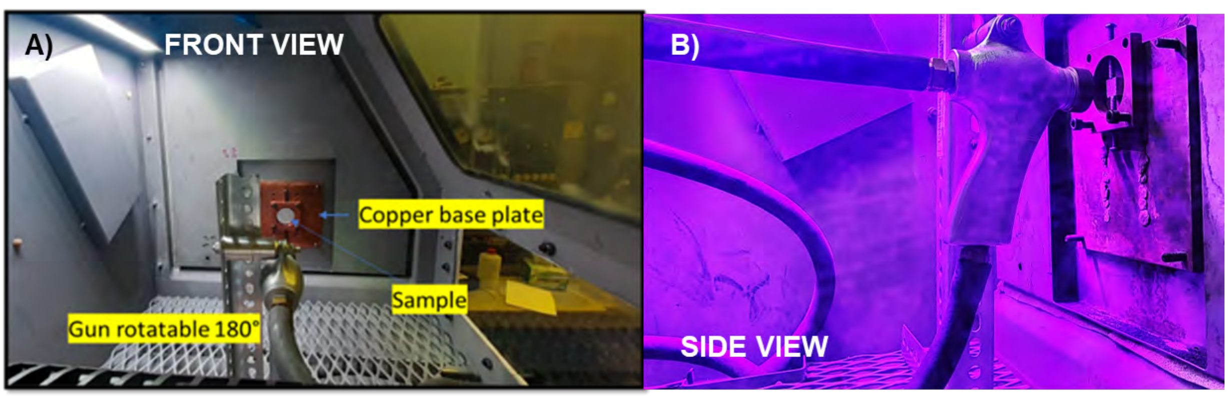

Figure S2 : (A) Front and (B) side view of gun and sample arrangement of planetary erosion test rig

2. Methods for Velocity Calculation and Energy Balance

2.1. Calibration and Scale Setup

To ensure accurate displacement and velocity measurements of particles, the high-speed video recordings were first calibrated using a reference object of known dimensions (e.g., a ruler or calibration marker) placed within the field of view. The videos were loaded into Pro-Analyst software (Xcitex, USA), and the scale was set by marking two points on the reference object. The known distance between these points was input into the software, allowing pixel-based measurements to be converted into real-world units (meters). This calibration was essential for accurately calculating particle displacements and velocities.

2.2. Particle Trajectory Tracking and Velocity Calculation

Particle trajectory tracking was performed using *Pro-Analyst software,* leveraging both automatic and manual tracking features. The software allowed frame-by-frame analysis of particle motion during impact events. For automatic tracking, the software identified and followed particles across successive frames based on their contrast with the background. In cases where automatic tracking was challenging due to noise or low contrast, manual tracking was employed to ensure precise measurements. The tracked particle positions were recorded for each frame, and the software computed the particle displacement (Δd) between frames. The time interval (Δt) between frames was determined by the camera's frame rate, allowing the particle velocity to be calculated using the following equation:

$$v = \frac{\Delta \mathrm{d}}{\Delta \mathrm{t}} \qquad \text{E}\textit{qn.1}$$

where vis the velocity (m/s), Δd is the displacement (m), and Δt is the time interval between frames (s). The velocity of each particle was computed based on its displacement across frames, using the scale and time interval established during calibration. The high-speed camera operated at a frame rate sufficient to capture particle motion at both 50 mph and 250 mph impact speeds. Pro-Analyst software recorded the velocity data in real-time as particles impacted the substrate or coating materials, providing accurate inputs for further kinetic energy calculations.

2.4. Kinetic Energy Calculation

The kinetic energy of each particle was calculated using the following equation:

$$KE = \frac{mv^2}{2}$$

Eqn.2

where KE is the kinetic energy (J), m is the particle mass (kg), and v is the particle velocity (m/s). The mass of each particle was determined based on its size and material density, which was known from the material properties of the erodent particles. For spherical particles, the volume was estimated as:

$$V = \frac{4\pi r^3}{3}$$

Eqn.3

Where r is the radius of the particle. The volume was then multiplied by the material's density to estimate the particle mass. The velocity data, derived from the particle tracking analysis, was then used to compute the kinetic energy at the point of impact.

2.5. Energy Absorption Measurement

Energy absorption by the coatings was calculated by comparing the kinetic energy of the particles before and after impact. For particles that rebounded from the surface, the velocity after impact was tracked using the same method, and the final kinetic energy (KEfinal)was calculated. For particles that embedded in the coating, the final kinetic energy was considered to be zero.

The absorbed energy was computed as:

$$\Delta E_{loss/abs} = \sum_{p=1}^{n} \frac{2}{3} \rho \pi {r_p}^3 \left({V_i}^2 - {V_r}^2\right) \qquad \textit{Eqn.4}$$

where Eabs is the energy absorbed by the coating , $\rho - particle\ density, r_p - particle\ radius, V_i - particle\ impact\ velocity, V_r - particle\ rebound\ velocity.$ This energy absorption was used to evaluate the impact resistance of APS and VPS coatings under varying impact velocities.

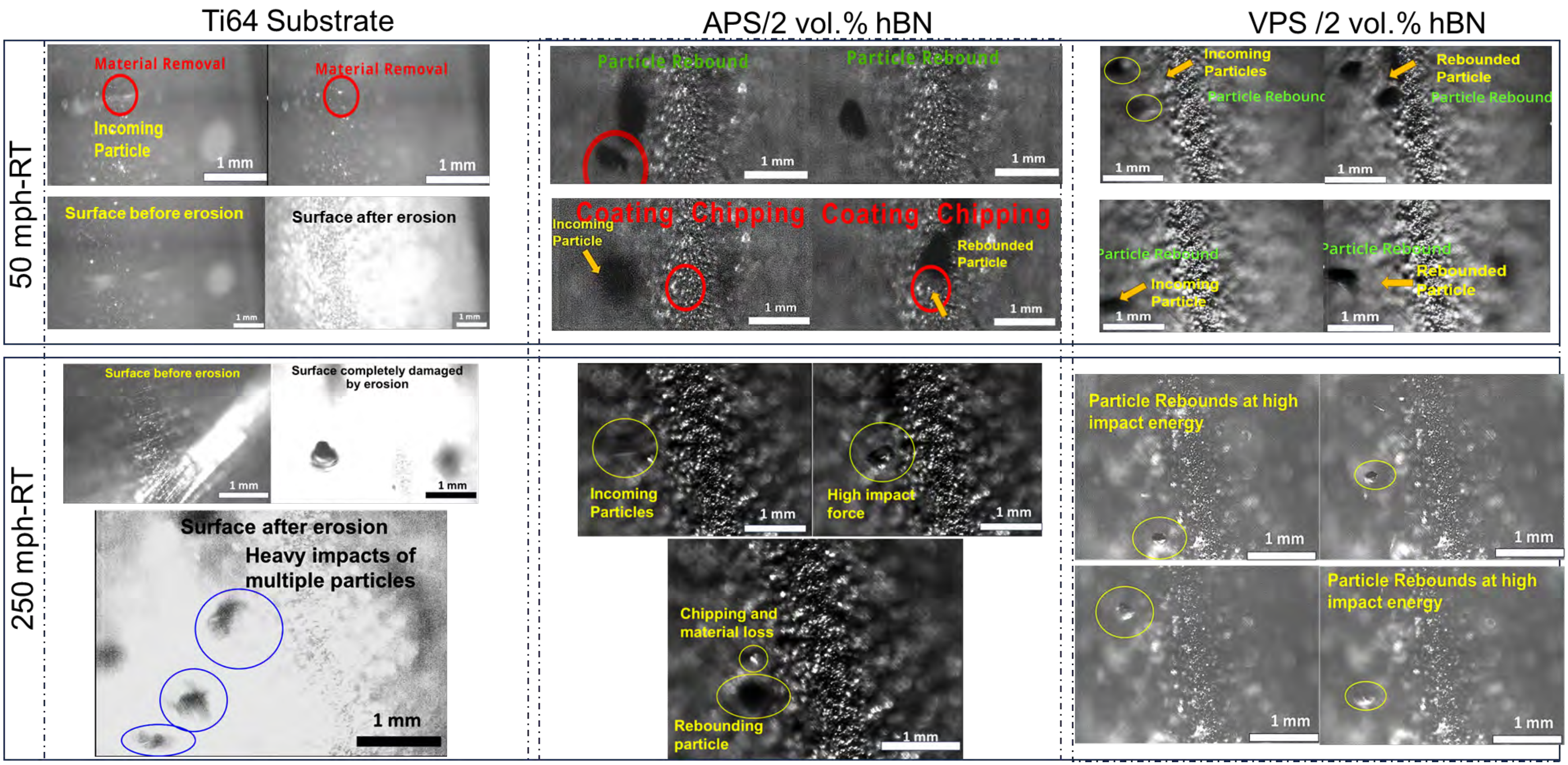

Figure S3: In-situ video snipshot of erosion mechanisms of Ti6Al4V substrate ,APS Ti/2 vol.% hBN coating and VPS Ti/2 vol.% hBN coating at 250 and 50 mph at RT

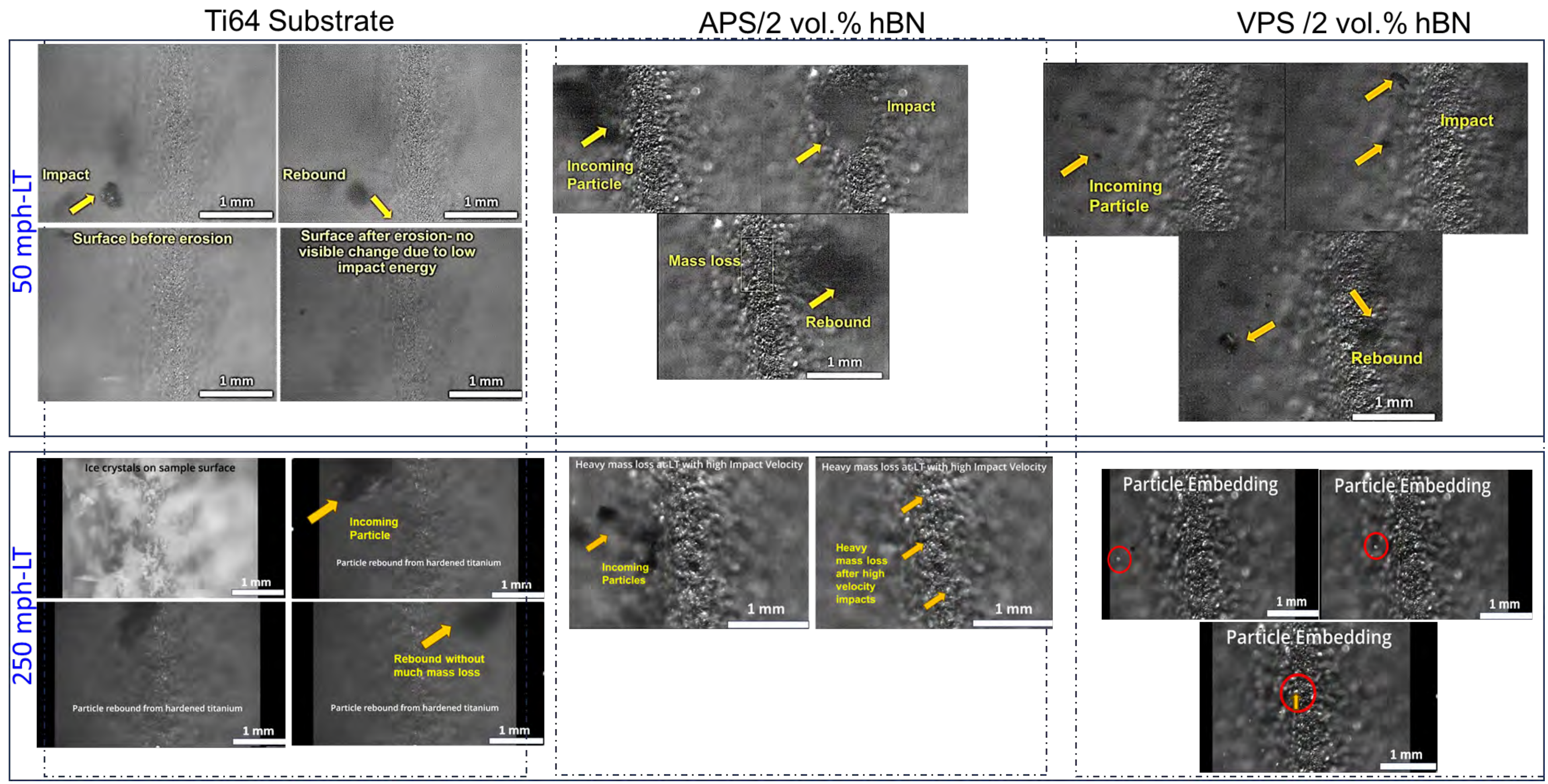

Figure S4: In-situ video snipshot of erosion mechanisms of Ti6Al4V Substrate ,APS Ti/2 vol.% hBN coating and VPS Ti/2 vol.% hBN coating at 250 and 50 mph at LT

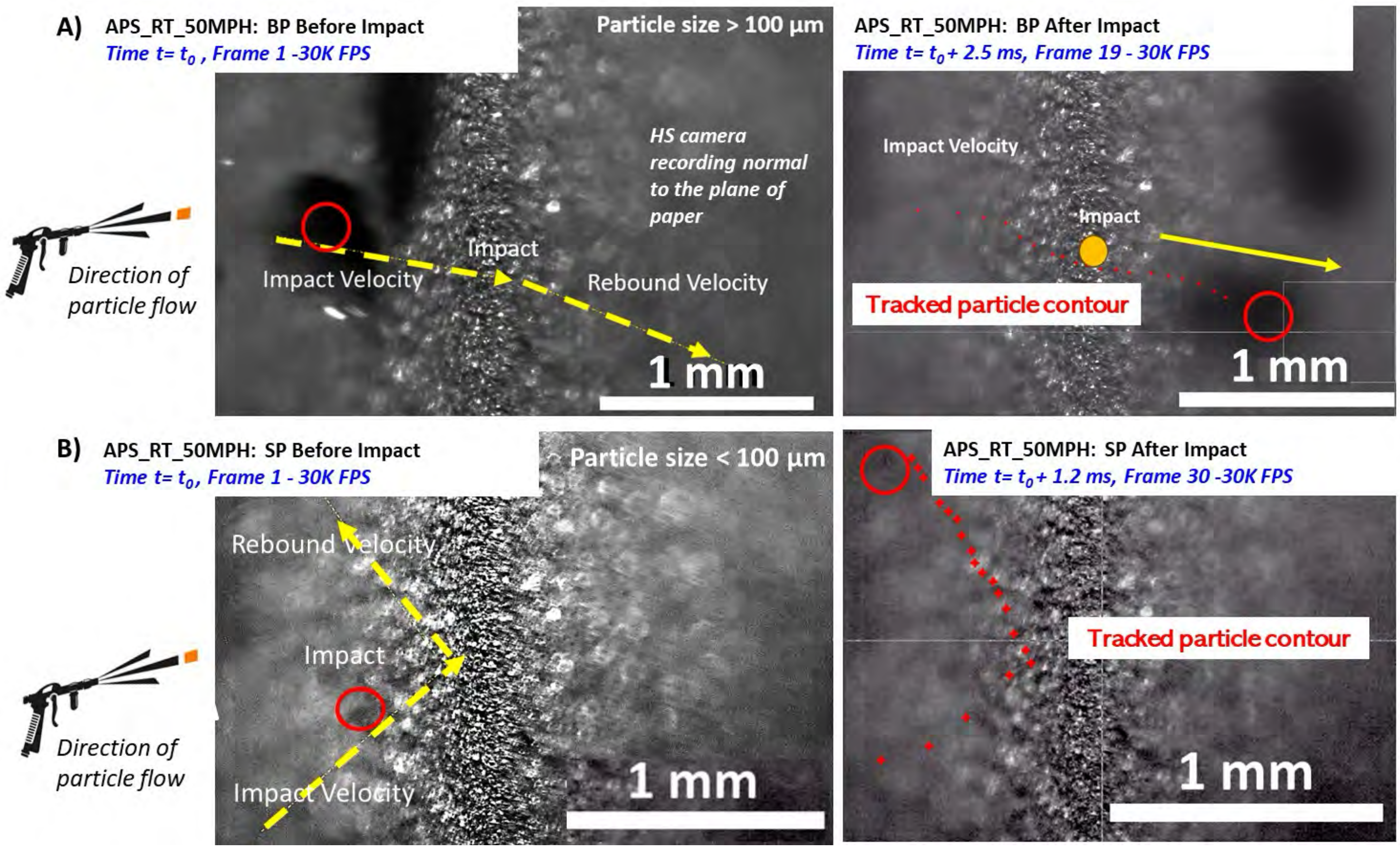

Figure S5: High-speed camera – Pro analyst analysis of particle tracking on the APS coatings at RT at 50 mph (A) Big particles (B->100 µm); (B) small particles (s-<100 µm)

Video Text Information

In-Situ Video S1 / Still 1: A comparative analysis of the impact behavior between the Ti substrate and VPS coatings at 50 mph. This video highlights the superior performance of the VPS coatings, showing less material deformation and wear compared to the bare Ti substrate.

In-Situ Video S2 / Still 2: A 250-mph impact test on the Ti substrate, where significant material loss is observed. The video showcases how the high-velocity impact results in severe erosion and damage to the uncoated Ti surface.

In-Situ Video S3 / Still 3: The effect of a 250-mph impact on APS Ti/2 vol.% hBN coatings, illustrating the chipping and failure of the coating. This video emphasizes the brittleness and reduced durability of the APS coating under extreme impact conditions.

In-Situ Video S4 / Still 4: A 250-mph impact test on VPS Ti/2 vol.% hBN coatings showing particle rebound. This video captures the enhanced energy absorption and impact resistance of the VPS coatings, as particles bounce off the surface without significant damage.

In-Situ Video S5 / Still 5: A close-up of the 250-mph impact on VPS Ti/2 vol.% hBN coatings, demonstrating particle embedding. This still provides insight into the coating's capacity to absorb energy and trap particles, enhancing erosion resistance compared to the uncoated substrate or APS coatings.